EXPERIMENTAL STUDY OF IMPURITY PRODUCTION

IN THE TOKAPOLE II TOKAMAK

by

NANCY SUSAN BRICKHOUSE

A thesis submitted in partial fulfillment of the

requirements for the degree of

DOCTOR OF PHILOSOPHY

(Physics)

at the

UNIVERSITY OF WISCONSIN-MADISON

1984

EXPERIMENTAL STUDY OF IMPURITY PRODUCTION

IN THE TOKAPOLE II TOKAMAK

Nancy Susan Brickhouse

Under the supervision of Professor Richard Norman Dexter

Impurities are introduced into tokamak plasmas by plasma bombardment of the surfaces, particularly in the presence of large sheath potentials. Since these impurities can grossly affect the plasma behavior, understanding and control of the production mechanisms are crucial to the achievement of clean discharges. Results of a study of impurity production on Tokapole II, a tokamak with a four-node poloidal divertor, are reported.

The release mechanism for low-Z impurities in Tokapole II has been characterized through impurity doping and isotopic exchange experiments. The desorption mechanism responsible for the low-Z impurity concentrations during the rise phase of the plasma current depends on the mass of the plasma ions. Doping with small amounts of any gas studied (H_2, D_2, He, N_2, O_2, Ne, Ar, Kr, and Xe) increases the early-time radiation of O, C, and N. For exotic gas doping this increase is linear with the dopant concentration, and proportional to the mass of the dopant, as expected for a momentum

transfer process. Isotopic exchange experiments confirm the mass-dependence of oxygen production.

A time-dependent coronal model is compared with the vacuum ultraviolet spectroscopic signals of the ionizing oxygen. The quantity σ/τ (desorption cross section divided by particle confinement time) is determined to be $4 \times 10^{13} cm^2/msec$. The oxygen influx has a large peak early in the start-up.

The ion-induced desorption is consistent with the edge potential and temperature measurements. These measurements indicate that the sputtering of aluminum during start-up should be negligible, as is observed. Instead aluminum is probably due to unipolar arcing; copper production is a combination of processes.

The recycling of impurities during the steady-state phase is discussed. Since the start-up phase is particularly active in producing impurities, and since the recyling impurities can be more effective than hydrogen in further production with their higher mass and charge, control of the start-up is important for impurity reduction.

ACKNOWLEDGEMENTS

I would like to thank my major professor, Richard N. Dexter, for his encouragement of this research project and for his sustained confidence in me. I appreciate the time he has spent and the useful criticisms he has made.

I thank Professors Clint Sprott, Stewart Prager and Jim Callen for discussions and suggestions in my research.

The technical crew on the Tokapole have provided the invaluable service of keeping the equipment operational. In particular, Tom Lovell's advice and general curiosity have helped to make the laboratory experience interesting. I thank Kay Shatrawka for her help in the production of this manuscript.

I am enormously grateful to my fellow graduate students. Don Holly, Arnie Kellman, Alan Biddle, Doug Witherspoon, and Dave Shepard have all given advice and encouragement. I thank Rich Groebner for doing the initial experiments in this area and for writing the thesis which has guided me through much of this work. In particular, I would like to thank Tom Osborne, who has spent many productive hours in discussion with me, and who has maintained a strong sense of doing physics properly. My collaboration with him has been a rewarding experience.

I would like to thank my parents, Mr. and Mrs. Robert Brickhouse, and other family and friends who have stood by me through my graduate career.

Finally, I thank my husband Andrew Szentgyorgyi for his love, understanding, and friendship. His enthusiasm for physics and for other pursuits has been inspiring.

Financial support has been provided by the United States Department of Energy.

TABLE OF CONTENTS

	Page
ABSTRACT	ii
ACKNOWLEDGEMENTS	iv
TABLE OF CONTENTS	vi
I. INTRODUCTION	1
A. Overview of the Impurity Production Problem in Tokamaks	1
B. Outline of the Results of this Research	6
II. TOKAPOLE II OPERATING CONDITIONS	11
A. Tokapole II - The Machine	11
B. Plasma Characteristics	25
C. Description of Impurities	36
III. ION-INDUCED DESORPTION DURING START-UP -- EXPERIMENTS	46
A. Impurity Doping Experiments	46
B. Isotopic Exchange Experiments	66
C. Intrinsic Impurity Doping Experiments	82
IV. ION-INDUCED DESORPTION DURING START-UP -- MODEL	93
A. The Time-Dependent Coronal Model	93
B. Experimental Parameters Used in the Calculation	97
C. Model of the Oxygen Influx	108
D. Discussion of the Influx Model and Desorption	113

V. PRODUCTION OF METAL IMPURITIES 130

VI. IMPURITY EVOLUTION DURING START-UP 158

A. Edge Parameters 159

B. Impurity Profile Evolution 173

VII. CONCLUSIONS AND DISCUSSION 187

A. Start-up 188

B. Steady-state 189

CHAPTER 1

INTRODUCTION

A. Overview of the Impurity Production Problem in Tokamaks

The working gas of present-day tokamaks provides a source for the desorption of low-Z (light) impurities and the sputtering of metal (heavy) impurities. Many possible mechanisms for introducing impurities are being studied: ion, electron, neutral, and photon induced desorption, thermal desorption, and chemical reactions to release light impurities, and evaporation, sputtering, blistering, and arcing to release metal impurities.[1]

Unipolar arcing and ion (or charge exchange neutral) sputtering are the major mechanisms for metal production in modern tokamaks. Usually arcing dominates during the start-up, while sputtering dominates during the steady-state.[2] The importance of the sheath potential between the plasma edge and the wall has been demonstrated both for arcing[3] and for sputtering.[4] The important mechanisms for light impurity production have been less well known experimentally. From theoretical considerations and from surface bombardment experiments in controlled environments, the dominant type of desorption for the relevant mass and energy ranges in a tokamak should be desorption induced by ions or charge exchange neutrals.[1,5]

After one to ten energy confinement times, the working gas may leave the central plasma region and reach the wall, where many processes may occur. Pumping by the wall (due to diffusion of the more energetic particles into the bulk solid) may cause a significant particle loss from the system. During the initial ionization phase, nearly half of the original filling gas is lost. In fact additional gas puffing throughout the discharge is necessary to maintain a steady-state electron density.[1] The early impurity build-up during this time of poor confinement indicates that there is a strong interaction with the wall. The working gas ions may knock adsorbed species from the wall or may reflect back towards the plasma. The series of processes by which plasma ions leave the plasma region, interact with the wall, and return to the plasma, through pumping, reflection, and desorption of additional working gas atoms is commonly referred to as recycling.

The relative importance of impurity recycling is not well understood. Potentially a small fraction of impurities may be a strong source of other impurities relative to hydrogen because of their larger mass and higher charge state, particularly if accelerated by a large sheath potential. A local density measurement of fully stripped oxygen on PDX has shown recently that the density of these highly charged ions at the limiter may be roughly 10% of their central density.[6] The energy of the ions hitting surface probes in the edge of PLT[7] and TFR[8] has also been found to be well above the expected ion temperatures based on the

electron temperatures there. The comparison between light and heavy impurity concentrations with concurrent measurements of the edge electron temperature under a variety of discharge conditions has given a qualitative understanding of ion sputtering in a tokamak. The presence of light impurities can contribute significantly to increased heavy impurity concentrations, as demonstrated on JFT-2;[9] however, on other machines, such as PLT, increased gas puffing cools the edge, reducing the energy of the bombarding ions, and thus reducing the heavy impurity concentration.[10] Models of the edge processes[11,12,13] account for both of these effects and for the relatively constant level of heavy impurities during a discharge. Working gas ion (and charge exchange neutral) sputtering is an important source;[14] nevertheless, a small percentage of light impurity ions can dominate the sputtering by two effects. Their larger mass gives them a larger momentum transfer to the wall for a given energy. Also, the multiply charged ions can gain more energy in the sheath potential. The impurity ions can thus cause an increase in sputtering, but only up to the point at which their radiative cooling of the edge reduces the sheath potential. Typical sheath potentials are on the order of sputtering thresholds, so that this edge cooling could actually eliminate sputtering.

Much progress is being made in understanding the details of these edge processes. Many machines are now making measurements of the relevant edge parameters.[15] Meanwhile, theoretical models for edge plasma transport, including atomic and molecular processes, the

plasma-wall interaction and impurity production mechanisms, and the particle flow with respect to boundaries such as limiters and divertors, are contributing to a comprehensive understanding of the edge physics.[16]

The deleterious effects of the plasma-wall interaction in a fusion reactor have been discussed at great length. The damage to reactor walls due to plasma and radiation bombardment and thermal load is of serious concern. Experiments at Columbia University were designed to simulate the effects of bombardment by a warm deuterium plasma on first wall material candidates. The plasma was given the energy flux expected at the first wall during one year of operation of a tokamak reactor. The materials tested showed blistering, melting, cracking, embrittlement,[17] and unipolar arcing.[18] The crucial problem to the fusion reaction itself is, of course, the ability of a small percentage (0.2 % tungsten) of partially stripped high-Z impurities to radiate all of the input energy, and thus prevent ignition.[19] Additionally, the start-up phase of a large tokamak such as TFTR must be designed to minimize the deleterious effects of low-Z as well as high-Z impurity radiation.[20]

In present tokamaks, impurities modify the density and temperature profiles not only by radiating power but also by adding electrons from multiply stripped ionic states, increasing the plasma resistivity, and altering transport processes. These effects in turn may alter the plasma stability behavior. The improvement in energy confinement with increased impurity levels (non-gettered

discharges) on ISX-B has been reported.[21] Divertor tokamaks with neutral beam heating have observed two new types of instability recently. Edge relaxation phenomena occurring during the H-mode, first reported by the ASDEX team, have been associated with high edge temperatures.[22] The achievement of this high confinement mode has been attributed to impurity recycling effects related to the divertor.[23,24] An internal mode, known as the fishbone instability, has been shown to limit the plasma beta.[25] These recently observed effects and the role played by impurities in them are not fully understood. The achievement of low safety factor q operation in Tokapole II may also be related to the divertor configuration and profile effects.[26]

Control of impurities is a major concern of all tokamaks. Material selection includes consideration of cleanliness, vacuum and mechanical properties, atomic number, and ability to withstand particle and thermal loads. For reactors the criteria will be even more stringent, as described in Reference 27. Conditioning procedures for walls and limiters, such as pulsed discharge cleaning,[28] titanium coating,[29], and glow discharge cleaning,[30] are used to eliminate the adsorbed water and carbon compounds as much as possible. Efforts to control the flow of impurities with divertors are being tested on several large tokamaks, particularly ASDEX, PDX, Doublet III, and DITE.[31] New limiter designs such as pumped limiters are also being investigated.[32] Greater understanding of the role of impurities at the edge and in the central current channel is

necessary for control of the minimal levels of impurities that will have to be tolerated in a reactor.

B. Outline of the Results of this Research

This thesis describes a series of experiments designed to characterize the impurity release mechanisms in Tokapole II. For one case, the early generation of the light impurities, a definite identification of the mechanism, ion-induced desorption, has been made. For this case a detailed study of the parameter behavior of the release mechanism in impurity doping and isotopic exchange experiments has been compared with a model of the time-dependent impurity influx. Additionally the edge parameters have been measured under a variety of start-up conditions, in conjunction with other start-up work performed on Tokapole II.[33] With a comparison to light impurity behavior during start-up, the identification of metal production mechanisms can be made tentatively as well. Secondary goals of the research have been to identify the impurity release mechanisms during the steady-state phase and to study the effects of impurities on the plasma behavior. The use of spectroscopic diagnostics to study the impurity behavior has followed closely the initial work on Tokapole II of R.J. Groebner.[34]

The major result of this research is the experimental description of the ion-induced desorption mechanism during start-up. A description of Tokapole II, the tokamak used for these experiments, with the present settings used for a standard

discharge, the plasma parameters for this typical case, and a summary of the impurity characteristics are presented in Chapter 2. The experimental data from the doping and isotopic exchange experiments are given in Chapter 3. This chapter shows the mass-dependent effects of dopant and working gases on light impurity concentrations. With the use of a time-dependent coronal equilibrium model to unfold the spectroscopic information, and the cross sections for desorption from the literature, one can model the influx of light impurities during start-up, as described in Chapter 4.

A description of experiments on the metal impurity production during start-up is given in Chapter 5. The information obtained about the initial impurity evolution then suggests interpretations of the start-up process. A discussion of this process and a presentation of data taken to examine the interrelated effects of the wall condition, the start-up procedure, and the plasma parameters in the edge follow in Chapter 6. Profile data are shown for some impurity states. Chapter 7 includes a summary of the research results, conclusions, and suggestions for further work.

REFERENCES

[1]G.M. McCracken and P.E. Stott, Nucl. Fusion 19 (1979) 889. This reference is an excellent review article on "Plasma-Surface Interactions in Tokamaks."

[2]G.M. McCracken, J. Nucl. Mater. 93/94 (1980) 3.

[3]H. Ohtsuka, M. Maeno, N. Suzuki, S. Konoshima, S. Yamamoto, N. Ogiwara, Nucl. Fusion 22 (1982) 823.

[4]R.J. Taylor and Lena Oren, Phys. Rev. Lett. 42 (1979) 446.

[5]W. Bauer, J. Nucl. Mater. 76/77 (1978) 3.

[6]R.J. Fonck, M. Finkenthal, R.J. Goldston, D.L. Herndon, R.A. Hulse, R. Kaita, and D.D. Meyerhofer, Phys. Rev. Lett. 49 (1982) 737.

[7]G.M. McCracken, S. Cohen, H.F. Dylla, C.W. Magee, S.T. Picraux, S.M. Rossnagel and W.R. Wampler, in: Proc. 9th European Conf. on Controlled Fusion and Plasma Physics, Oxford, 1979, Vol. 1 (1979) 89.

[8]G. Staudenmaier, P. Staib, R. Behrisch and Equipe TFR, Nucl. Fusion 20 (1980) 96.

[9]N. Suzuki, N. Fujisawa, S. Konoshima, M. Maeno, M. Shimada, T. Yamamoto, S. Kasai and K. Uehara, in: Proc. 9th European Conf. on Controlled Fusion and Plasma Physics, Oxford, 1979, Vol. 1 (1979) 90.

[10]S. Suckewer and R.J. Hawryluk, Phys. Rev. Lett. 40 (1978) 1649.

[11]S.A. Cohen, H.F. Dylla, S.M. Rossnagel, S.T. Picraux and C.W. Magee, J. Nucl. Mater. 76/77 (1978) 459.

[12]H. Ohtsuka, Nucl. Fusion 22 (1982) 827.

[13]G.M. McCracken, S.J. Fielding, and H. Ohtsuka, J. Nucl. Mater. 111/112 (1982) 396.

[14]S.J. Fielding and A.D. Sanderson, J. Nucl. Mater. 93/94 (1980) 220.

[15]See, for example, Sections 2 and 3 on Plasma Edge Experiments in: J. Nucl. Mater. 111/112 (1982).

[16]See the recent review article by D.E. Post, D.B. Heifetz, and M. Petravic, J. Nucl. Mater. 111/112 (1982) 383.

[17]R.A. Gross, B. Jensen, J.K. Tien, and N. Panayotou, in Plasma-Wall Interactions (Proc. Int. Symp. Julich, 1976) Pergamon Press, New York (1977) 659.

[18]J.K. Tien, N.F. Panayotou, R.D. Stevenson, and R.A. Gross, J. Nucl. Mater. 76/77 (1978) 481.

[19]D.M. Meade, Nucl. Fusion 14 (1974) 289.

[20]R.J. Hawryluk and J.A. Schmidt, Nucl. Fusion 16 (1976) 775.

[21]R.C. Isler, B.A.P.S. 28 (1983) 1053.

[22]F. Wagner et al., Phys. Rev. Letts. 49 (1982) 1408.

[23]ASDEX team, B.A.P.S. 28 (1983) 1052.

[24]R.J. Fonck, B.A.P.S. 28 (1983) 1052.

[25]K. McGuire et al., Phys. Rev. Letts. 50 (1983) 891.

[26]T.H. Osborne and N.S. Brickhouse, University of Wisconsin Plasma Studies PLP 908 (1983).

[27]H. Vernickel, J. Nucl. Mater. 111/112 (1982) 531.

[28]L. Oren and R.J. Taylor, Nucl. Fusion 17 (1977) 1143.

[29]P.E. Stott, C.C. Daughney, and R.A. Ellis, Nucl. Fusion 15 (1975) 431.

[30]H.F. Dylla, S.A. Cohen, S.M. Rossnagel, G.M. McCracken, Ph. Staib, presented at 26th National Symposium of the American Vacuum Society (1979).

[31]M. Keilhacker and K. Lackner, J. Nucl. Mater. 111/112 (1982) 370.

[32]P. Mioduszewski, J. Nucl. Mater. 111/112 (1982) 253.

[33]D.J. Holly, S.C. Prager, D.A. Shepard, and J.C. Sprott, Nucl. Fusion 21 (1981) 1483.

[34]R.J. Groebner, Ph.D. Thesis, University of Wisconsin (1979).

CHAPTER 2

TOKAPOLE II OPERATING CONDITIONS

A. Tokapole II - The Machine

Tokapole II has been operated as a four-node poloidal divertor tokamak for the experiments described in this thesis. These experiments have been performed over the period from March 1979 to April 1983. The Tokapole II device has been described in more detail elsewhere.[1,2] The aluminum vacuum vessel is a torus with a 44 cm square cross section and a 50 cm major radius (Figure 2-1). Four internal rings of 5 cm minor diameter, supported inside the tank (Figure 2-2), are used to generate the divertor configuration. The solid rings are made of a high conductivity chromium-copper alloy; the support rods are made of a beryllium-copper alloy.

The vacuum poloidal field (Figure 2-3) is created by currents in the rings, driven inductively by a 7.2 mF, 5 kV (90 kJ) capacitor bank through an iron core transformer. The 40:1 turns ratio on the transformer gives a sinusoidal field shape in time which has a half period of 5.6 ms. The poloidal field is generally crowbarred actively, by adding a 450 volt, 0.96 F (97 kJ) capacitor bank. In the spring of 1981, a damping resistance was added to the primary circuit for the standard operating procedure in order to shorten the initial voltage spike. Figure 2-4a shows the resulting poloidal gap

Figure 2-1. Tokapole II.

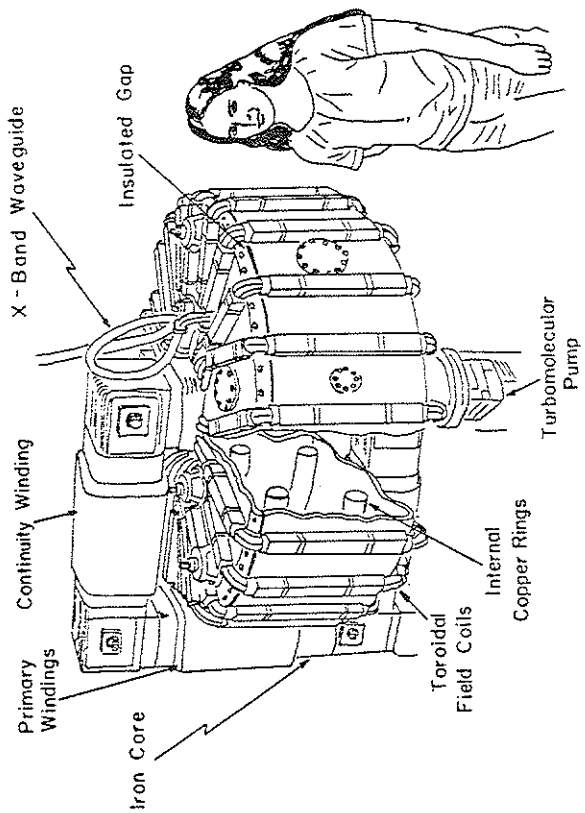

Figure 2-1

Figure 2-2. Cross section of vacuum vessel showing internal rings.

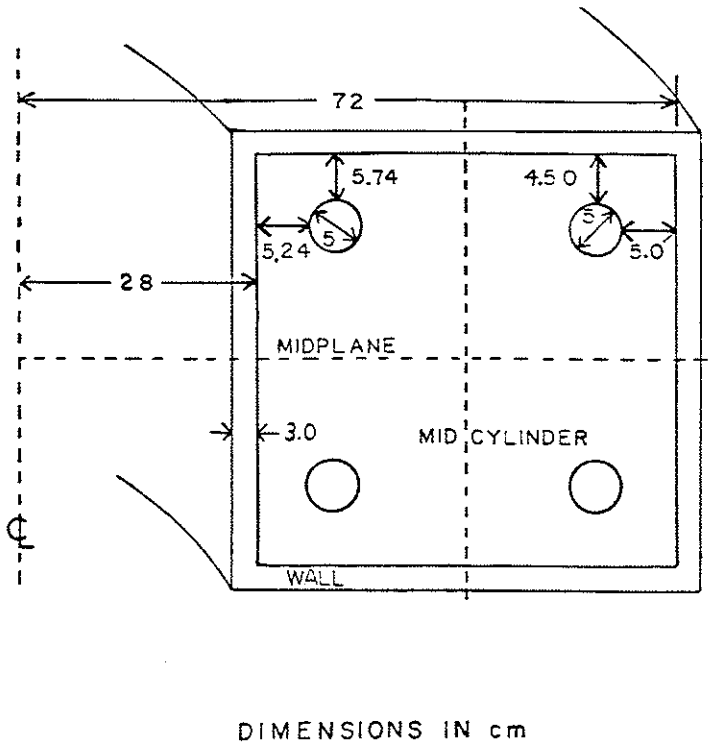

Figure 2-2

Figure 2-3. Vacuum poloidal magnetic field flux plot. The major radius R is measured from the center of the torus. The vertical scale is measured from the center of the vacuum vessel. Dimension are in m.

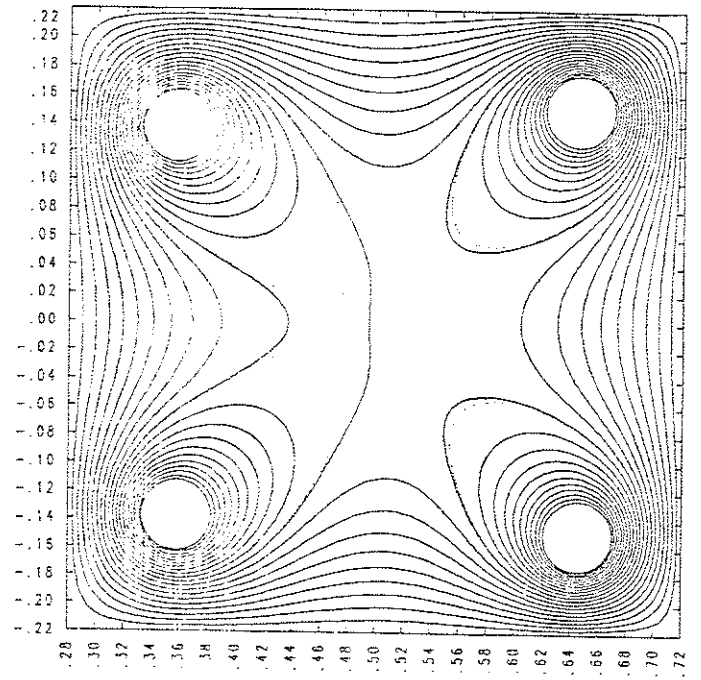

Figure 2-3

Figure 2-4a. Timing of poloidal gap voltage. Discharges prior to February 1981 were made without damping resistance. Since 1981 standard discharges have used damping resistance.

Figure 2-4b. Timing of toroidal magnetic field.

Figure 2-4

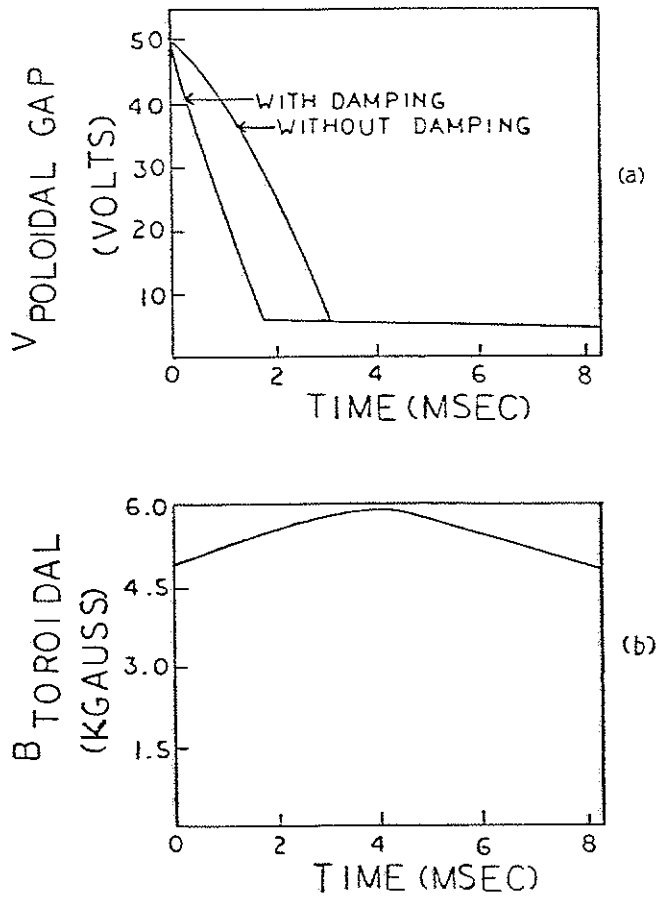

voltages produced. The total flux available in the core is 0.15 webers. Since image currents of the ring currents flow in the 3 cm thick conducting walls, the magnetic symmetry should be improved over machines with non-conducting walls. At the poloidal gap, continuity windings return the wall currents around the transformer core. The vertical positions of the rings may be varied $\pm$ 5.0 mm to change the position of the vacuum field null. The existence of the null allows for some plasma current to start up away from the walls. The equilibrium of the plasma is quite sensitive to the position of the rings as well.

The toroidal field, $B_{toroidal}$ (Figure 2-4b), is created by external windings driven by 52 mF, 5 kV (650 kJ) capacitor bank. The half period is about 10 msec. The image currents in the conducting walls produce uniform toroidal field in the machine despite the widely spaced field windings. The field is passively crowbarred near peak field, which has been gradually increased from about 4 kG to 6 kG as the standard operating field on axis.

During the course of these experiments, many vacuum pumping and wall conditioning systems have been used. In 1979, both a turbomolecular pump and a helium cryogenic pump were used to maintain base pressures in the low 10^{-7} to high 10^{-8} torr range. The walls were baked to 75°C overnight and cooled to <50°C during the day. The wall conditioning procedure used overnight was a pulsed discharge cleaning technique, demonstrated by Taylor to be effective in removing surface contaminants.[3] Since 1980 the cryopump

has been abandoned, originally for long-term maintenance, and also now for additional port access for diagnostics. The bake/cool cycling has not been operational for the last few years due to known air leaks opening in the triple joint (where the toroidal and poloidal gaps meet) during temperature cycling. The machine is currently held at about 50°C. In early 1980, overnight pulsing was replaced by glow discharge cleaning in hydrogen.[4] For Tokapole II the procedure consists of biasing the rings positive with respect to the wall with a high voltage (roughly 300 to 400 V) and filling the tank with about 30 mtorr of extremely pure hydrogen. At the present settings, the wall draws a positive current of about 120 mA whereas the rings draw about 60 mA of negative current. Many configurations have been used in the past, including a long run with higher current to the rings, which may have resulted in copper sputtering. Glow discharge cleaning had two immediate advantages, due to its more intense conditioning of the vacuum surfaces. A marked improvement in the discharge parameters was observed in general, and the deleterious effects of air venting the machine were minimized. With an overnight glow, the machine could produce reasonable discharges the day after an air venting, whereas pulsed discharge cleaning had taken about a week to achieve normal operation. Currently there is concern that continued glow discharge cleaning is having some bad effects as well, primarily because of the sputtering of copper from the rings to all surfaces. A new pulsed discharge cleaning system and a titanium coating scheme (which would also improve the base

pressure) are being designed, and should be operational soon. Initial experiments have indicated that a combination of the three procedures, with minimal glow discharge cleaning to avoid sputtering copper, should produce reasonable wall conditions.

The chamber is filled to 3×10^{-4} torr with the working gas, usually hydrogen, prior to the field pulses. A fast piezoelectric puff valve is used. Additional gas may be puffed during the discharge, either in stages with fixed amplitudes, or with a feedback circuit which has a time response of about 1 msec and is controlled by the line-averaged ion saturation diagnostic in the edge region. Microwave pre-ionization at the electron cyclotron frequency (ECRH) can be used to aid the start-up. Three types of sources are available: a continuous 100 W S-band (2.45 GHz), a pulsed 10 kW X-band (9 GHz), and two pulsed 5 kW K-band (16.5 GHz), with pulse lengths of 500 μsec. An applied d.c. vertical field can also be used to produce 10 Gauss on axis. This field seems to push the magnetic axis, which usually sits out a few cm, back towards the center, particularly for discharges with low plasma current.

Scrape-off plates may be inserted up to the separatrix (Figure 2-5) from all four sides at one toroidal azimuth; however, for the research presented in this thesis, the Tokapole has been operated without scrape-off plates. Roughly one-third of the plasma current flows in the common flux region (the region enclosing all four rings) during start-up. A study of edge parameters during the steady-state has been made recently[5] for the two cases; the impurity

Figure 2-5. Central current channel separated from common flux or scrape-off region by separatrix (dashed line). Four scrape-off plates, or limiters, may be inserted to the separatrix. For the limiter cases discussed here only three scrape-off plates were used, with their extension into the tank approximately as shown.

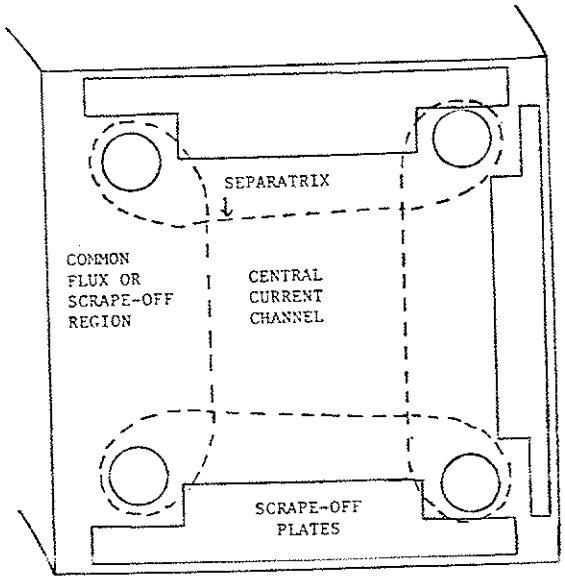

THE TOKAPOLE II DIVERTOR CONFIGURATION

Figure 2-5

profiles observed spectroscopically are consistent with the measurements.

B. Plasma Characteristics

In this section the basic plasma parameters as measured by various diagnostics are reviewed. Since the plasma-wall interaction experiments have been conducted over a wide range of discharge conditions, the data presented in this section are intended to be representative of the plasma parameters. The impurity production mechanisms have been essentially the same throughout the variations of magnetic fields, base vacuum pressures, cleaning techniques, and other parameters.

In the spring of 1979 Tokapole II had been in operation for about one year, during which time reasonable operating parameters and cleanliness had been achieved, although the discharge duration was only about 4 msec. Data from these short-lived discharges can be found in References 2 and 6. Since then the discharge length has been increased to 12 msec (15 msec maximum achieved) by conditioning the vacuum vessel walls, increasing the toroidal field, and using late gas puffing. The peak T_e and $\bar{n}_e$ have not been significantly improved; however, the major accomplishment has been the achievement of several msec of steady-state operation. The energy confinement time is now about 0.5 msec, roughly in accord with tokamak scaling.[7]

A theoretical poloidal magnetic field flux plot[8] is shown in Figure 2-6 for standard toroidal field and current. Both square and dee-shaped equilibria have been measured with magnetic probes.[9] The discharge can be divided into two time phases: the start-up phase, roughly the first 1.5 to 2.5 msec, during which peak current and density occur and the plasma heats up to its peak temperature, and the plateau or steady-state phase, during which the parameters are essentially constant until the plasma runs out of volt-sec. Figures 2-7 and 2-8 illustrate the plasma behavior for two different poloidal gap voltages, with all other parameters fixed.

The plasma current is difficult to determine accurately since it is only about 20% of the current in the rings. The routine plasma current monitor estimates the total plasma current by measuring the poloidal gap voltage and the current in the transformer primary, and modeling the plasma as an element in the ohmic heating transformer secondary. This monitor is accurate to about 25% during steady-state, as verified with a large Rogowski coil,[2,10,11] but overestimates the start-up current near the walls by as much as a factor of two. The plasma current monitor gives the peak I_p between 30 and 50 kA, with 10 to 25 kA during the steady-state phase. (Figures 2-7a and 2-8a).

The initial gas concentration, measured with a Bayard-Alpert Fast Ionization Gauge, is equivalent to 1×10^{13} cm^{-3} of fully ionized H_2 gas. The peak of the line-average electron density, $\bar{n}_e$ (Figures 2-7b and 2-8b), measured with a 70 GHz microwave

Figure 2-6. Poloidal magnetic flux plot calculated with an MHD equilibrium code. This case is representative of the higher I_{plasma}, $B_{toroidal}$ plasmas. The dotted lines are the separatrices.

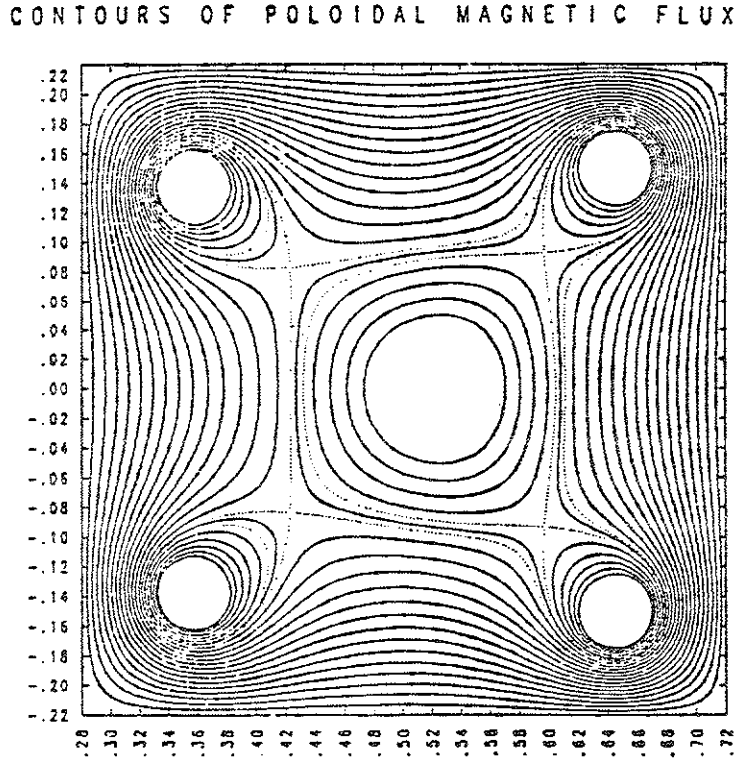

Figure 2-6

Figure 2-7a. Plasma current versus time for a standard discharge with higher peak current, using $V_{poloidal\ gap}$ and $B_{toroidal}$ of Figure 2-4. This case is represented by the theoretical flux plot of Figure 2-6. The measurements shown in this Figure are for the same shot.

Figure 2-7b. Line-average electron density versus time.

Figure 2-7c. Central chord SXR signal versus time, showing the time of the T_e peak.

Figure 2-7d. Ion saturation current density measured with a line-average Langmuir probe in the edge. This signal represents the edge density and is used for the late gas puffing feedback circuit.

Figure 2-7a and 2-7b

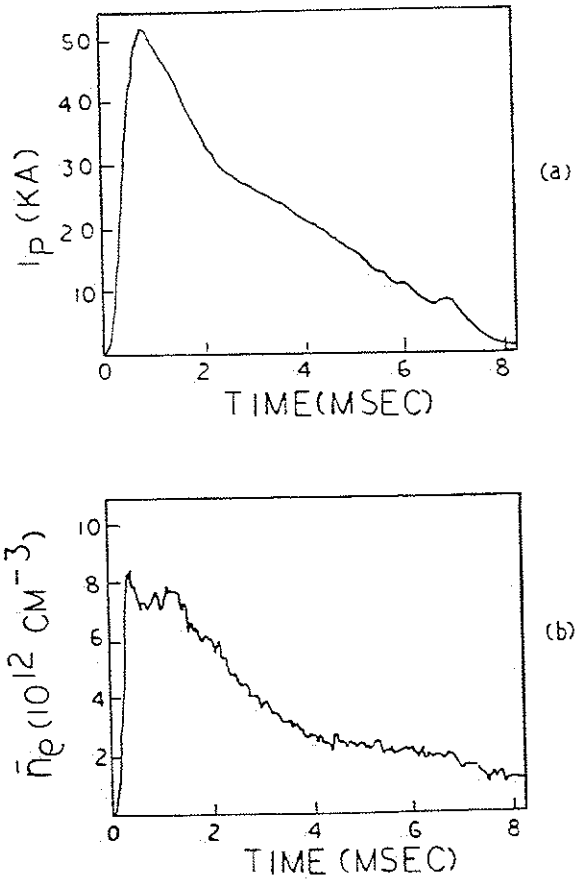

Figure 2-7c and 2-7d

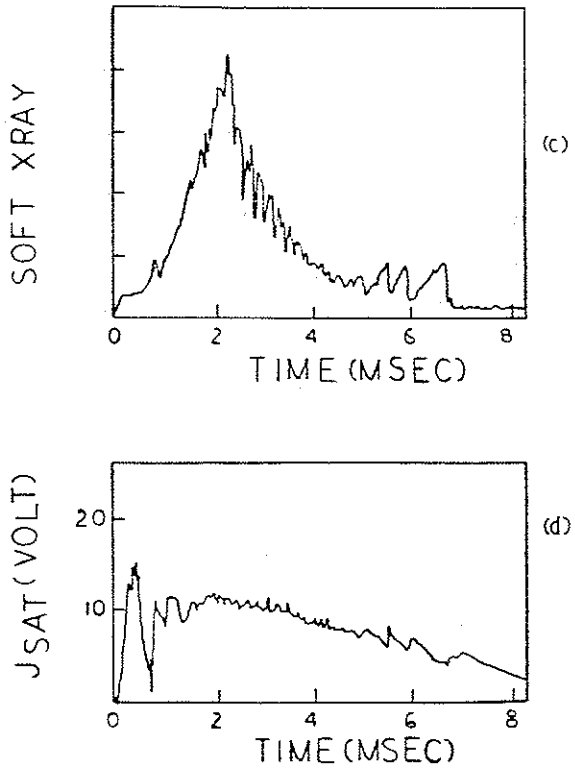

Figure 2-8a. Plasma current versus time for a lower $V_{poloidal\ gap}$ than in Figure 2-7. All other settings are the same as for Figure 2-7. All measurements shown in this Figure are for the same discharge.

Figure 2-8b. Line-average electron density versus time.

Figure 2-8c. Central chord SXR signal versus time.

Figure 2-8d. Edge ion saturation current density versus time.

Figure 2-8a and 2-8b

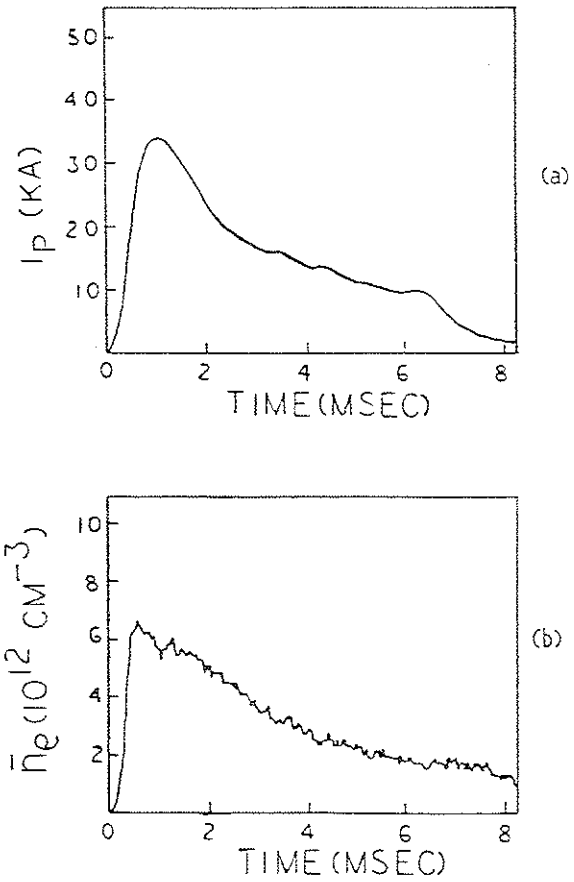

Figure 2-8c and 2-8d

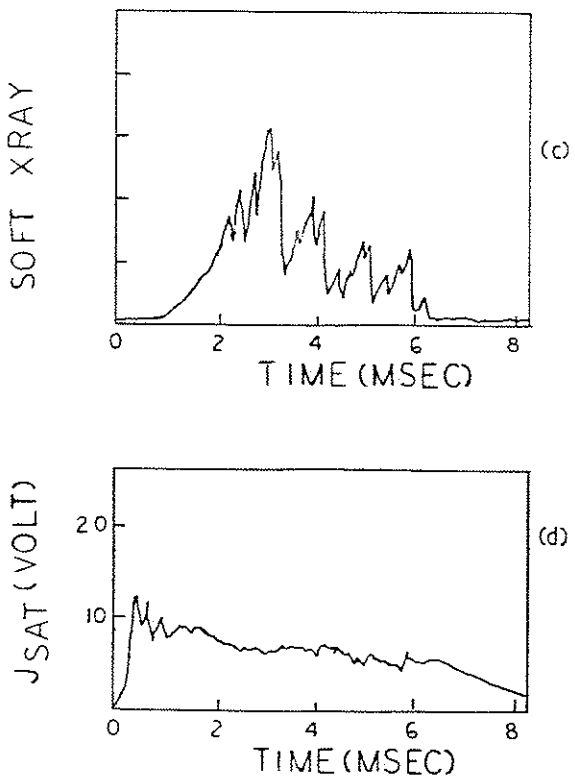

interferometer viewing the midcylinder from the top of the machine, is 6 to 8 x 10^{12} cm^{-3} at 0.3 to 0.4 msec, dropping to a steady-state value of 2 to 3 x 10^{12} cm^{-3}. The peak of the electron temperature, T_e, has been estimated to be about 100 eV by two techniques. A spectroscopic measurement of the oxygen series line radiation in the Vacuum Ultraviolet (VUV) with an absolutely calibrated 1-m Seya VUV monochromator, in combination with a time-dependent coronal model, gives the time evolution of T_e during the start-up phase.[12] The conductivity temperature measured by current density and toroidal electric field probes has given rough agreement for Z_{eff}, the effective ionic charge of the plasma, of 2.5 to 3.0. The electron temperature peaks between 2 and 3 msec, as illustrated by the central chord soft xray (SXR) emission (Figures 2-7c and 2-8c). The SXR detectors are surface barrier diodes with polypropylene filters which limit the transmission to the energy range 60 eV to 300 eV. The detectors have approximately an exponential dependence on T_e for Tokapole energy ranges.[13]

A routine diagnostic for edge densities and temperatures is the three-tipped line-average Langmuir probe located on the vacuum separatrix between the lower ring and the outer wall. The edge density is represented by the probe measurement of ion saturation current density, J_{SAT}, in the common flux region (Figures 2-7d and 2-8d).

C. Description of Impurities

Spectroscopic measurements of impurity radiation have been made using an absolutely calibrated 1-m Seya VUV monochromator which views a chord through the center of the plasma, a VUV survey system consisting of a 1/2-m Seya spectrometer with a microchannel plate in its exit plane, capable of time-gated operation in the 400-1300 Å region of the VUV, and two 1/2-m Jarrell-Ash visible monochromators with tilting capabilities. A tiltable integrated VUV detector and an array of SXR detectors provide spatial information on the impurity radiation as well as total power radiated in these regions. These diagnostics are described in more detail elsewhere.[2,12,14] For routine monitoring of impurity levels a set of four photomultipliers is mounted on the top of the machine with filters for visible radiation. A grazing incidence monochromator for observation of the wavelength region between the VUV and the SXR regions is currently being tested.

During the first year of operation the Tokapole discharge parameters improved significantly, primarily due to a decrease in the impurity levels with discharge cleaning. Since then, and for the duration of this research, the concentration of impurities during the start-up has remained essentially the same. The line radiation for these standard discharges is less than 25% of the ohmic input power and thus cannot be the dominant energy loss mechanism. The low-Z impurity concentrations have been estimated by

an impurity doping method (described in Chapter 3). The major low-Z impurities are oxygen (2×10^{11} cm^{-3}), carbon (5×10^{10} cm^{-3}), and nitrogen (3×10^{10} cm^{-3}). For the metal impurity concentrations, primarily aluminum and copper, an estimate has been made by comparing the low-Z impurity contribution to the integrated VUV radiation. The metal impurities must then account for about 40% of the VUV radiation.[12] Major impurity lines, measured photographically with the VUV survey spectrometer and output to the densitometer in the U.W. Biochemistry Department, are shown in Figure 2-9 for the start-up phase.

The impurity ion radiation observed on tokamaks is characterized by two distinct behaviors: an ionization peak during the start-up phase, when ohmic heating of the volume causes the burnout from lower to higher ionization states, and a plateau level, when each ionic state peaks its profile at the location where T_e is roughly one-third of its ionization potential.[15] Groebner presents data from the spring of 1979 with distinct ionization peaks, but with plateau levels similar in magnitude to the peaks and often with second peaks as well. (See Reference 2, p.129.) Although the start-up impurity levels have remained similar, a large improvement in the plateau behavior has occurred. The plateau levels are now low and extremely constant in time. The time-dependent signals of several bright impurity lines are shown in Figure 2-10. The improvement can be attributed both to a decrease of local sources from unconditioned wall or ring areas and to a decrease in the

Figure 2-9. A sequence of pictures obtained for consecutive discharges with the VUV survey instrument microchannel plate. The gate is on in each case for 0.4 msec. These pictures illustrate the evolution of the VUV spectrum with time from bottom to top.

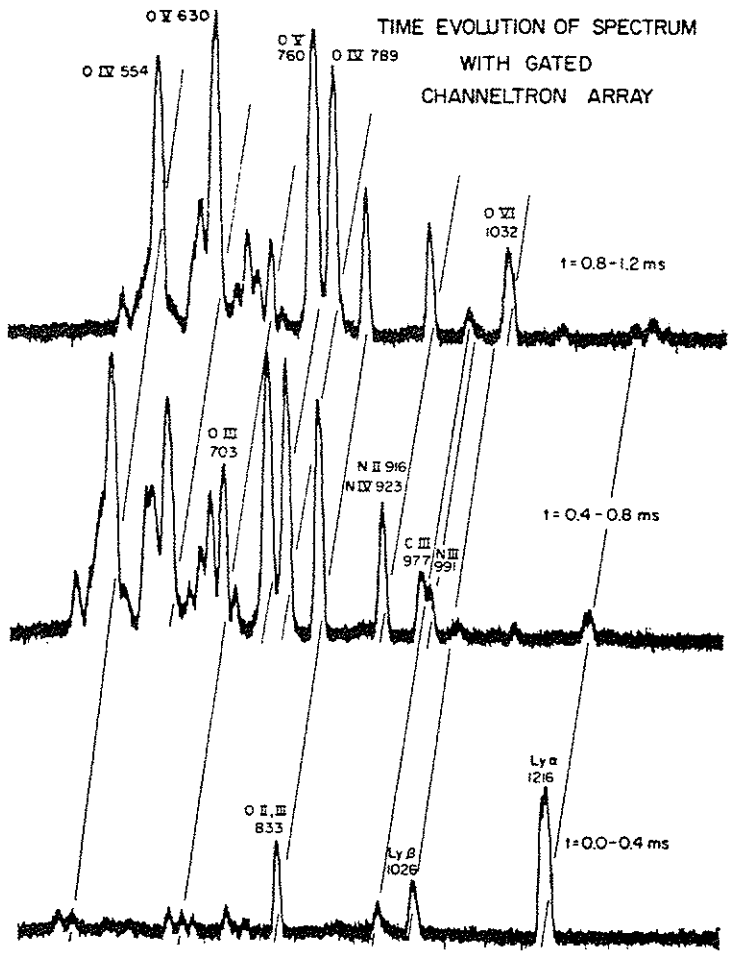

Figure 2-9

Figure 2-10a. Impurity line radiation versus time for a standard discharge. (The end of the discharge at 12 msec is not shown.) This data was taken with the 1-m Seya VUV monochromator. Several important impurity lines are shown.

Figure 2-10b. Impurity line radiation versus time for the same discharge of Figure 2-10a. This data was taken with the routine impurity monitor with filtered photomultipliers.

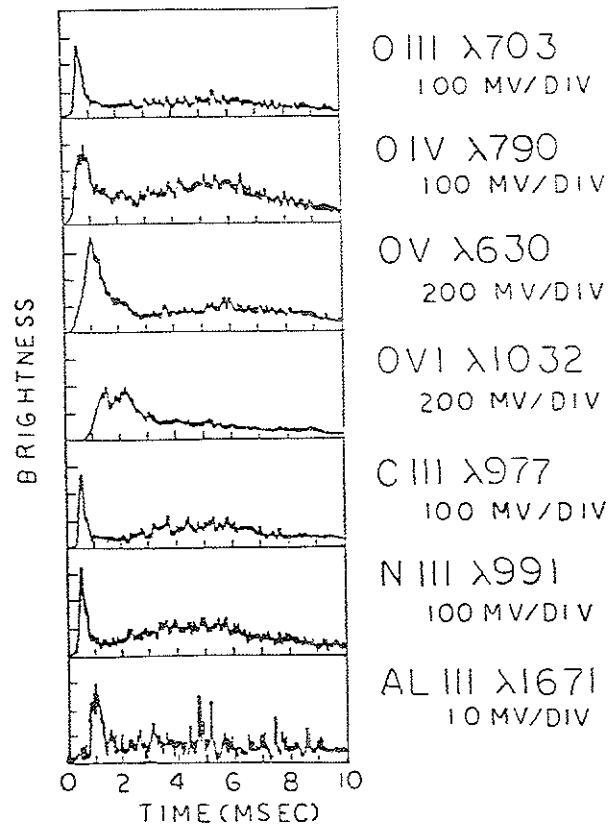

Figure 2-10a

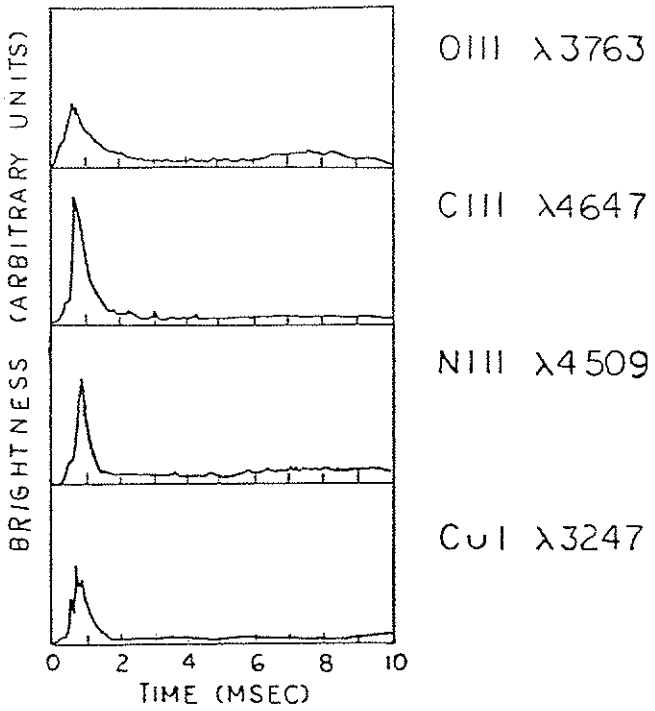

Figure 2-10b

impurity influx. The decrease in influx may imply an improvement in particle confinement (consistent with a measured improvement in the energy confinement time), which may be effectively an improvement in the plasma's ability to shield its hot central core from the plasma boundary region, where rapid recycling must certainly occur.

REFERENCES

[1]J.C. Sprott, University of Wisconsin Plasma Studies PLP 744 (1978).

[2]R.J. Groebner, Ph.D. Thesis, University of Wisconsin (1979).

[3]L. Oren and R.J. Taylor, Nucl. Fusion 17 (1977) 1143.

[4]H.F. Dylla, S.A. Cohen, S.M. Rossnagel, G.M. McCracken, and Ph. Staib, "Glow Discharge Conditioning of the PDX Vacuum Vessel," presented at the 26th National Symposium of the American Vacuum Society, New York (1979).

[5]T.D. Rempel and G.A. Emmert, University of Wisconsin Plasma Studies PLP 894 (1983).

[6]A.P. Biddle, R.N. Dexter, R.J. Groebner, D.J. Holly, B. Lipschultz, M.W. Phillips, S.C. Prager, and J.C. Sprott, Nucl. Fusion 19 (1979) 1509.

[7]J.C. Sprott, University of Wisconsin Plasma Studies PLP 877 (1982).

[8]M.W. Phillips, University of Wisconsin Plasma Studies PLP 765 (1978).

[9]B. Lipschultz, S.C. Prager, T.H. Osborne, J.C. Sprott, and M. Phillips, Phys. Rev. Lett. 43 (1979) 36.

[10]J.C. Sprott, University of Wisconsin Plasma Studies PLP 712 (1977).

[11]S.C. Prager, J.C. Sprott, T.H. Osborne, and K. Miller, University of Wisconsin Plasma Studies PLP 756 (1978).

[12]R.J. Groebner and R.N. Dexter, Plasma Physics 23 (1981) 693.

[13]R.J. Groebner and R.N. Dexter, University of Wisconsin Plasma Studies PLP 770 (1978).

[14]R.N. Dexter and R.J. Groebner, University of Wisconsin Plasma Studies PLP 768 (1978).

[15]T.F.R. Group, Plasma Physics 20 (1978) 207.

CHAPTER 3

ION-INDUCED DESORPTION DURING START-UP -- EXPERIMENTS

A. Impurity Doping Experiments

This section describes the experimental procedure and results for the doping experiments. The major result of these doping experiments is that the generation of the light impurities, oxygen (O), carbon (C), and nitrogen (N), increases with the concentration of any doped gas such that this increase per dopant atom is proportional to the dopant mass. This result implicates ion-induced desorption as the major process for introducing light impurities into Tokapole II plasmas. Many dopant gases (D_2, He, CH_4, N_2, O_2, Ne, Ar, Kr, and Xe) have been used for this series of experiments, during which impurity line radiation signals for O, C, and N have been observed.

The dopant gas is added to a fixed concentration of the working gas, usually hydrogen. The hydrogen puff valve is opened 16.7 msec before the discharge starts in order to allow time for uniform filling of the machine. For higher mass gases the dopant gas puff valve must be opened even earlier, with a typical delay of 25 msec between this valve opening and the poloidal field triggering. A maximum delay of 40 msec has been used for the series including Xe, the heaviest dopant gas used. The timing is usually set so that the

fast ionization gauge, used to measure the gas concentrations, reads the peak of the dopant gas signal prior to the hydrogen puff. The calibration of the gauge for different gases uses the coefficients of Lewin[1] and Dushman.[2] The line radiation signals for the exotic gas dopants are proportional to the concentration measured by the ionization gauge.

Doping with any gas causes radiation signals from all light impurities to increase, as shown in Figure 3-1. The largest increase is during the impurity ionization phase, with a small increase, if any, during the plasma current plateau. Figure 3-2 illustrates the early time-dependence of the effects of 2% Ar concentration on the OIII λ703 line radiation signal. As the dopant concentrations increase the line radiation signals also increase. For dopant levels up to those levels needed to double the spectral line intensities of the ionization peak (dopant concentrations less than 10% of atomic H concentrations) the increase is linear, except for self-desorption, although higher dopant levels lead to nonlinearity (see Section C). The increase in the ionization peaks with added hydrogen gas is shown in Figure 3-3. Typical data for an impurity doping series are shown in Figure 3-4.

The data of Figure 3-4 suggest that the impurity levels depend not only on the dopant concentration, but also quite strongly on the dopant mass. In order to assess the error in assuming that changes in line radiation signals reflect changes in the impurity ion concentrations in the plasma, the relative changes in n_e and T_e over

Figure 3-1. Densitometer trace of VUV spectrum with no doping (bold line) and for Ar doping (light line), using the time-gated spectrometer (gated on between 0.5 and 1.0 msec). This Figure illustrates the increase of light impurities with doping. The nonlinearity of the photographic emulsion prevents this technique from being used for quantitative measurements; instead, monochromators with photomultipliers are used.

Figure 3-1

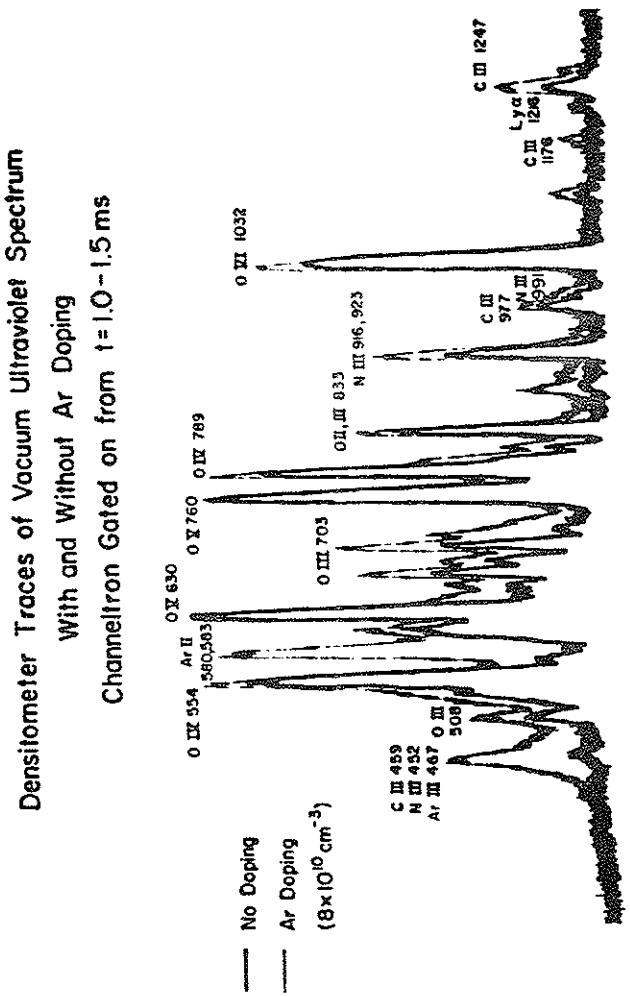

Figure 3-2. OIII λ703 signal as a function of time during start-up for cases with and without doping.

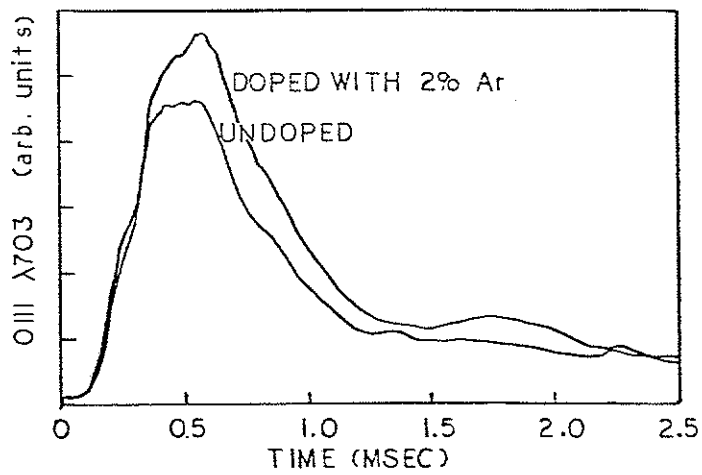

Figure 3-2

Figure 3-3. OIII λ703 and NIII λ4511 versus added H, for a puffed H concentration of about 9.8×10^{12} atoms/cm^3 and a peak interferometer density of 4.2×10^{12}/cm^3.

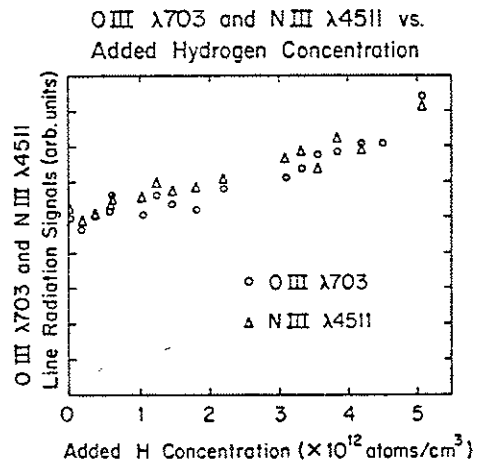

Figure 3-3

Figure 3-4. OIII λ703 ionization peak as a function of dopant concentration for various dopant gases. For Ar, the set of data points is shown. The error bars on the point on the He plot show the typical shot to shot variation for a data point.

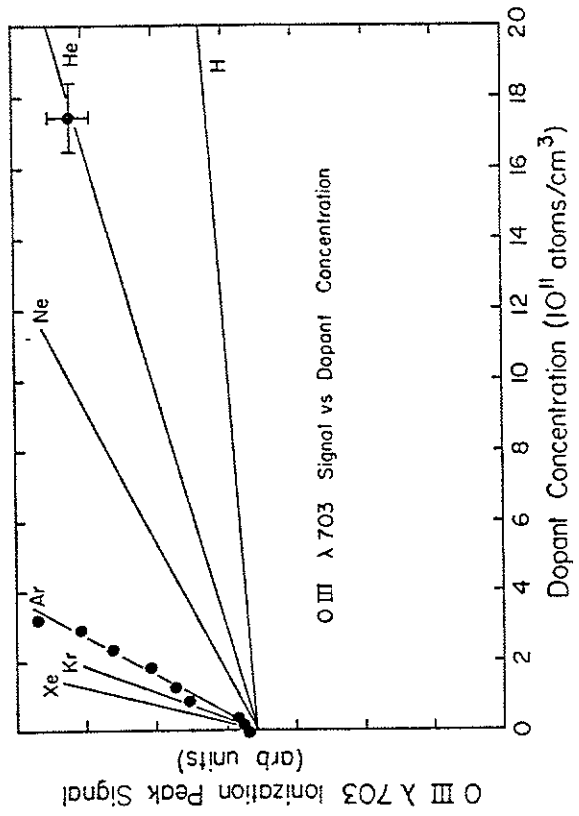

Figure 3-4

a doping run must be determined. The impurity line radiation signals are proportional to $n_e n_i Q(T_e)$, where Q depends on the ionic state. From microwave interferometer and probe measurements of n_e during doping, the change in n_e accounts for less than 20% of the increase in the impurity radiation. Figure 3-5 shows that OIII increases significantly faster than $\bar{n}_e$ with N doping.

With the VUV monochromator and SXR detectors an estimate of the change in T_e caused by doping can be made. Temperature profile modifications and changes in the rate of increase of T_e during current channel buildup, as well as decreases in the peak T_e, may all contribute to changes in impurity line radiation with doping. Two methods used to estimate the volume-averaged $T_e(t)$ are: a separation of the strong T_e-dependence of SXR signals from the weaker dependence on n_e and n_i by comparison with the integrated VUV and interferometer, and a coronal model of the oxygen series, OII through OVI[3] (see Chapter 4). The coronal model fits $T_e(t)$ for the undoped plasma to the time evolution of the oxygen ionic states. T_e increases up to about 20 eV by about 200 μsec, remains flat until OIII peaks between 600 and 800 μsec, then rises sharply to 130 eV by the SXR peak time at 2.5 msec, as shown in Figure 3-6. For the maximum dopant concentration used (which doubles OIII), the coronal model fit for T_e shows little effect for the 20 eV phase, but shows that T_e can peak up to 350 μsec later at 100 eV. The magnitude of the SXR changes agrees well with the measured $\bar{n}_e$ change and the T_e change found from the model. The relative increase in the SXR

Figure 3-5. A comparison of line radiation signal and electron density as measured with a microwave interferometer. This Figure shows that the increase in n_e is not a significant contribution to line radiation signal increases. (OIII signal is porportional to $n_e n_i Q(T_e)$.) This plot includes high dopant levels.

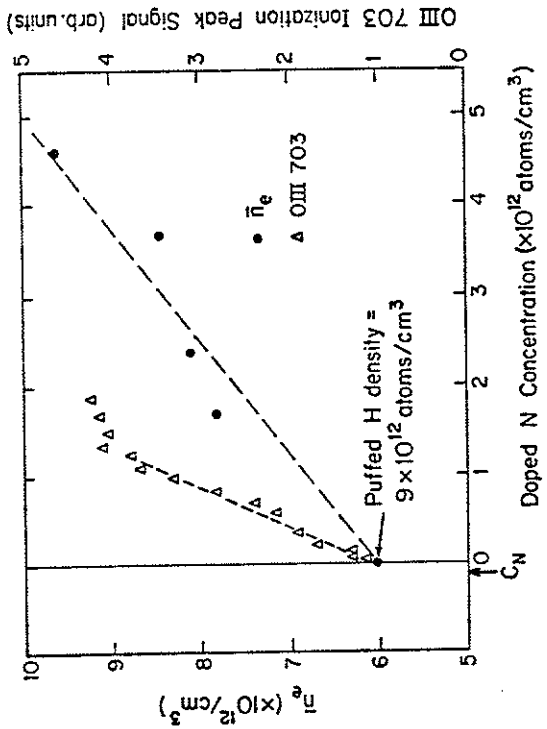

Figure 3-5

Figure 3-6. Simulations for $T_e(t)$ based on coronal model of oxygen series data for cases with and without doping. (See Chapter 4.)

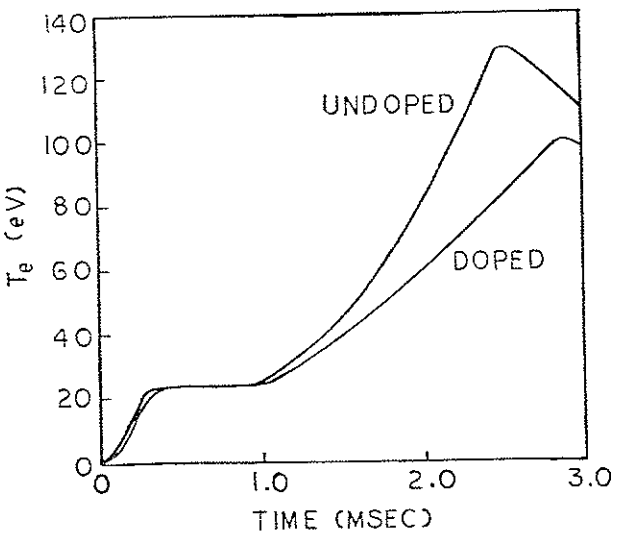

Figure 3-6

signal for early times is less than the relative increase in VUV radiation. Both signals are proportional to the line-averaged product $n_e n_i$ but SXR is a strong function of T_e, whereas VUV has only a weak dependence on T_e.

For small changes in n_e and T_e, then, a linear increase in impurity line radiation implies a proportional increase in the impurity concentration. The error in this proportionality factor is estimated by comparing the increase in various oxygen series lines during doping. The increases per dopant atom of OII λ797, OIII λ703, OIV λ789, and OV λ630 are within a factor of two of each other, as shown in Figures 3-7 and 3-8. Different dopants tend to produce changes in the oxygen radiation in the same way. Most of the mass-dependence studies have used the lower ionization state OIII (also NIII, CIII) for several reasons. The function $Q(T_e)$ for OIII λ703 is only weakly dependent on T_e. The peak time of OIII varies the least with doping, unlike OVI, which peaks 300 to 400 μsec later for modest doping. The time variation of the OVI λ1032/1036 ionization peak is shown on Figure 3-8, indicating its strong T_e dependence. Also the effects of any additional influx of oxygen during the start-up phase are minimized by observing the earlier time signal. Visible lines are available to check the VUV lines. The visible lines OIII λ3763, CIII λ4647, and NIII λ4509 are proportional to the respective VUV lines OIII λ703, CIII λ977, and NIII λ991 at the ionization peak during doping.

Figure 3-7. Ionization peak signals as a function of puffed H concentration for the oxygen ionic states OII through OVI. The signals are normalized to 1.0 at an H concentration of 1.8 X 10^{13} atoms/cm^3. (These plasmas have an electron density of about 1 X 10^{13} cm^{-3}.)

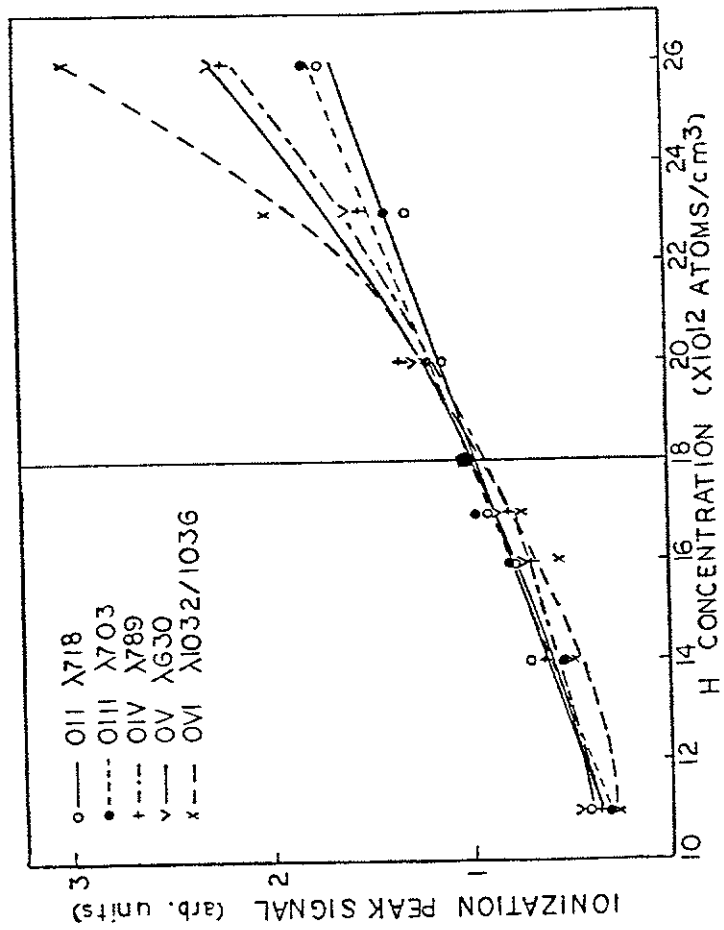

Figure 3-7

Figure 3-8. Ionization peak signals as a function of doped Ar concentration for the oxygen ionic state OII through OVI, taken on the same run as Figure 3-7. The puffed H concentration is 1.8 X 10^{13} atoms/cm^3. For this Figure, two sets of ionization peak times are indicated: for OVI next to the X's, and for OIII next to the solid circles.

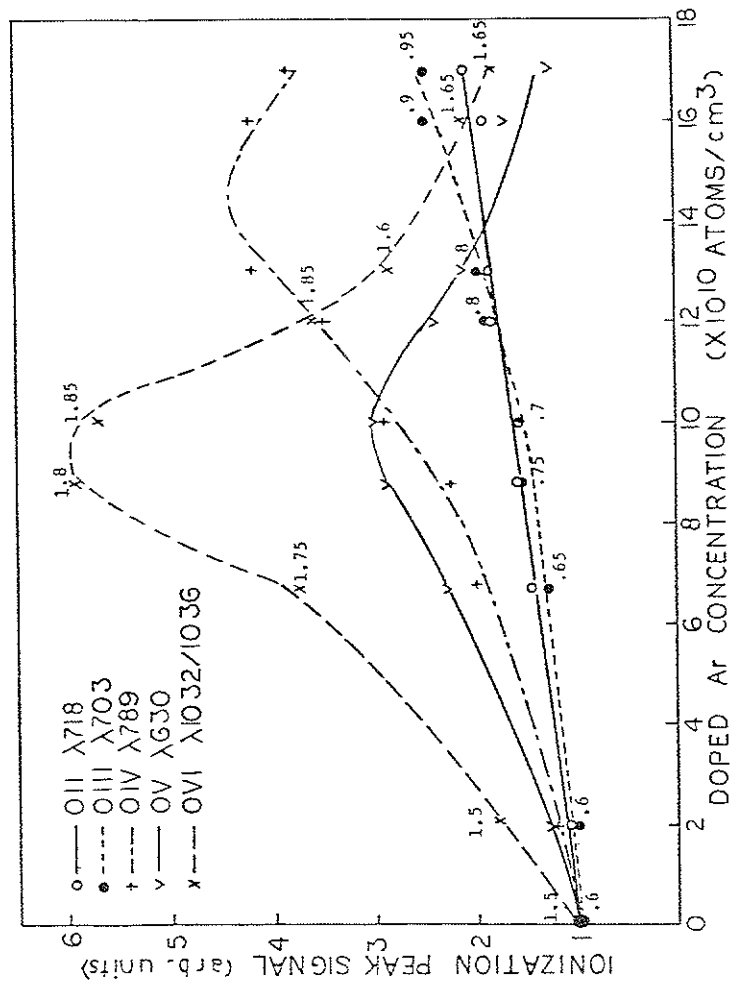

Figure 3-8

Thus, the increase of impurity concentration per dopant atom is roughly proportional to the mass of the dopant. The normalization with respect to the effect of adding hydrogen provides a reference signal for different plasma conditions. The mass variations, shown in Figure 3-9, are similar for OIII, CIII, and NIII. These data summarize the results of the doping series taken (about seven different runs with three to five dopant gas series per run). The error bars thus represent the changes in the mass proportionality factor with changes in machine conditions and plasma parameters. The reproducibility of the impurity production is fortunately quite good. The extent to which the signals represent the impurity concentrations is estimated to be of this same order.

From the mass proportionality shown in these Figures, a momentum transfer process involving the initial plasma ions is implied. Electron- and photon-induced desorption and chemical reactions can play only a minor role in the production of light impurities. The behavior of the plasma ions during start-up is discussed in more detail in the next few chapters.

B. Isotopic Exchange Experiments

In order to estimate the importance of hydrogen-induced desorption relative to intrinsic impurity-induced desorption, we have observed working gas (H_2 and D_2) recycling in studies similar to recycling studies in DITE and other machines.[4,5,6,7,8] This type of experiment has been commonly used to distinguish between the two

Figure 3-9. The relative impurity signal increase for OIII λ703 (a), NIII λ4511 (b), and CIII λ4647 (c) versus the dopant mass (for atoms). The open circles do not represent linear increases (see Section C).

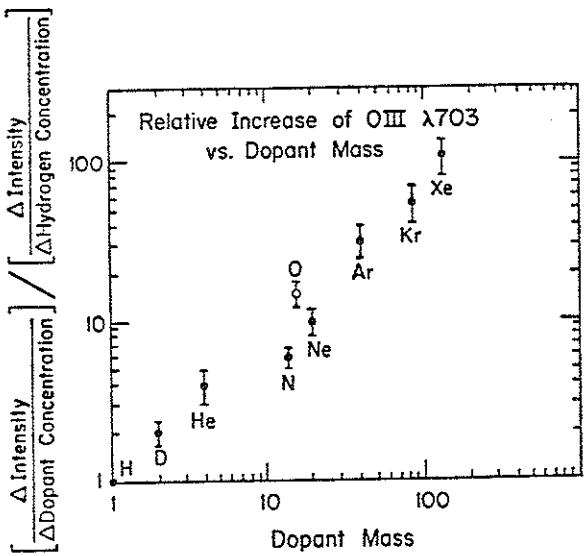

Figure 3-9a

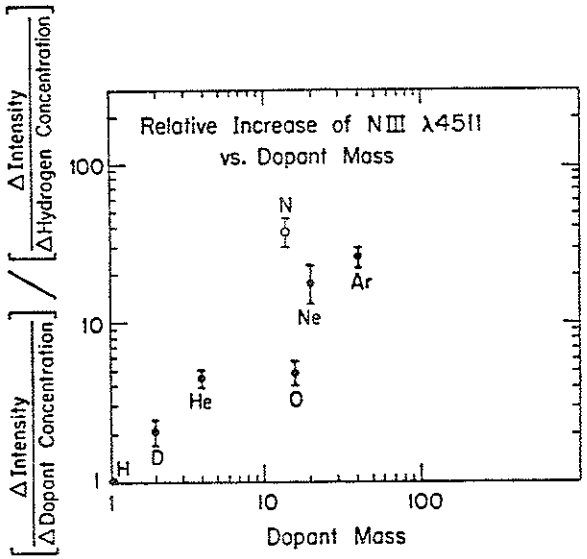

Figure 3-9b

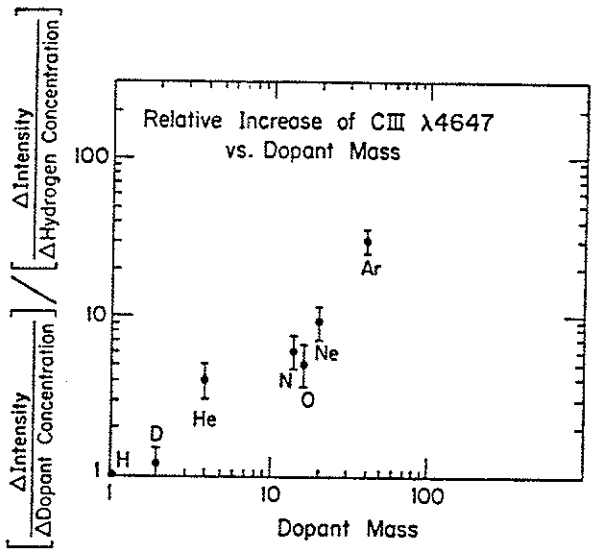

Figure 3-9c

components of the discharge gas, the initially puffed gas and the gas released from the wall. Typically the amount of gas in the tokamak wall is several orders of magnitude larger than the density in the plasma. This gas can diffuse from within the solid to the surface, where it is easily desorbed by the plasma, so that the initially puffed gas can exchange with the wall gas during the course of the discharge. Since the particle confinement time is less than the discharge length this recycling process involves several exchanges with the wall during the course of a discharge. (This description is, of course, oversimplified since tokamaks now generally use additional gas puffing during the discharge to control the recycling process and to keep the density constant. No late gas puffing has been used for these experiments.) The question of particular interest here is the effect of isotopic exchange on impurity levels.

The discharges in Tokapole II had been run almost exclusively in H_2 prior to this experiment. Figure 3-10 shows the change in the plasma constituents after switching the working gas to deuterium. The line radiation signals for H_β and D_β, separated by using slits for 0.3 Å resolution on the visible monochromator, are used to compare the start-up and plateau behavior. For these neutral hydrogen and deuterium lines, the ionization peaks occur at 300 μsec, and the levels are flat by about 500 μsec, so that these signals give a comparison between early and late start-up. The early and late time signals are normalized to be the same for the

Figure 3-10. H_β λ4861 and D_β λ4860 versus number of shots after switching the working gas from H_2 to D_2. The scales for the peaks and plateaus have been normalized to be the same for the first shot. There may be a discrepancy in comparing the intensity of H_β to D_β.

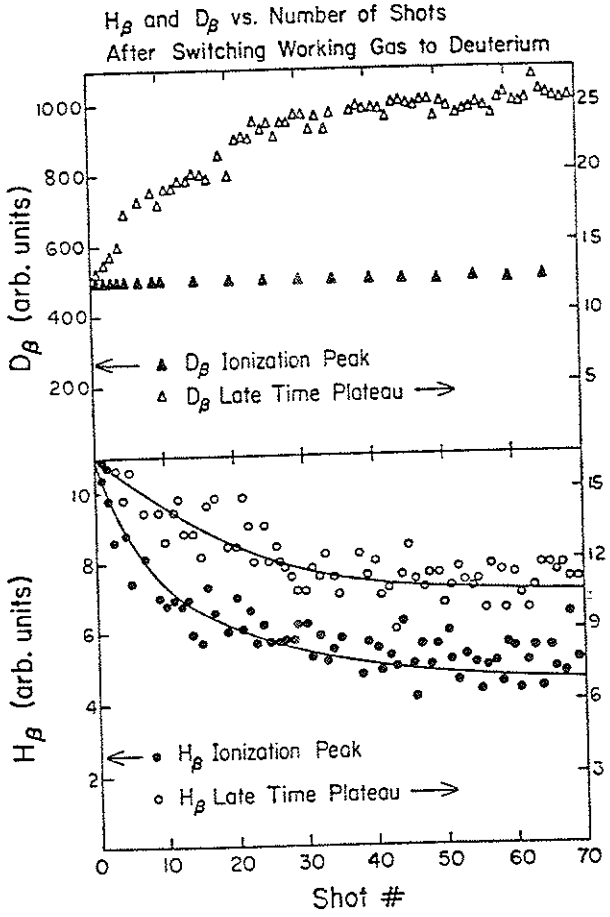

Figure 3-10

first shot. The D_β ionization peak signal is constant during these shots, since, of course, the initial puff is the same throughout these shots and constitutes the dominant discharge gas. The D_β plateau increases gradually to approach a constant level supplied partially from the wall. The hydrogen level in the plasma decreases to approach a constant non-zero level (there is always plenty of H in the system from residual water and hydrocarbons), with the ionization peak decaying somewhat more rapidly. Thus, the initial D plasma has already knocked a substantial amount of H from the wall by 300 μsec. The faster decay of the H_β ionization peak presumably indicates that the most easily desorbed H is replaced by D during the first several shots.

Figure 3-11 shows the effects of switching the working gas back to H_2. The behavior of the wall gas is slightly different from the previous case. For the first several shots the D_β ionization peak and the plateau decay at the same rate; later, the ionization peak begins to decay less rapidly than the plateau. This result seems somewhat inconsistent but may be explained by the difference in the amount of diffusion into the bulk solid between H and D over the short time of D_2 filling and in an environment with residual H_2. The D_β results are reproduced in Figure 3-12 with the additional data from the residual gas analyzer to show the decay of D_2 between shots. The slow decay to zero level is an indication that diffusion of D into the solid has occurred over the short duration of running in D_2.

Figure 3-11. H_β and D_β versus number of shots after switching the working gas back from D_2 to H_2, immediately after the run of Figure 3-10.

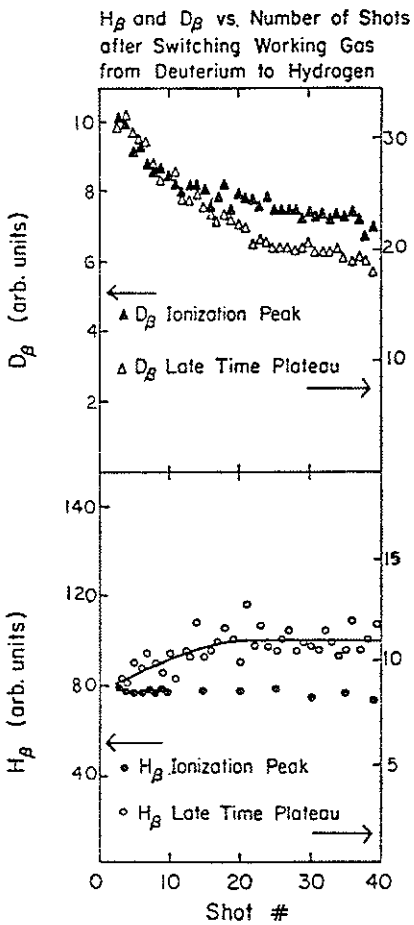

Figure 3-11

Figure 3-12. The D_β results from Figure 3-11 plotted with data from the residual gas analyzer (RGA) between shots.

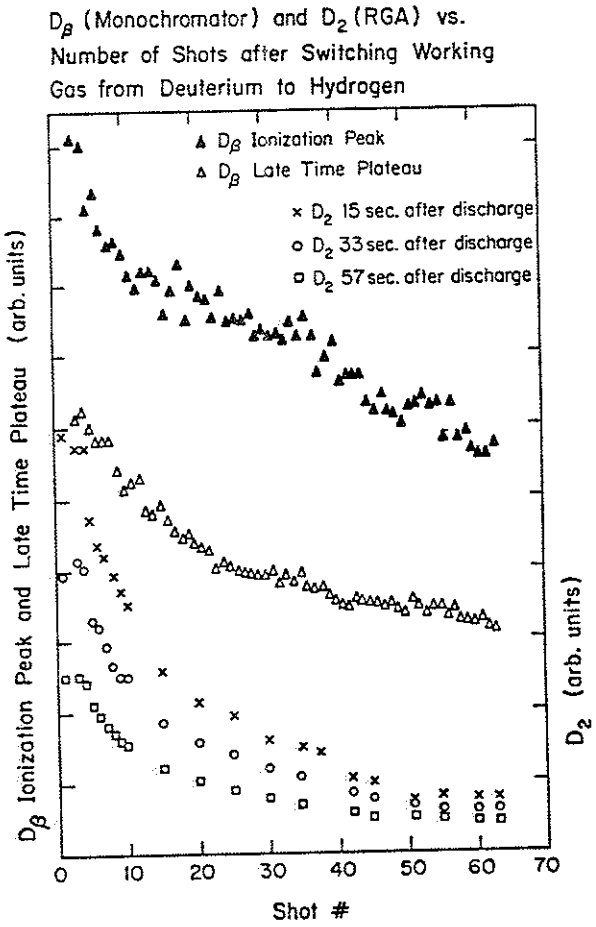

Figure 3-12

For a similar run the OIII λ703 ionization peak shows a dependence on the working gas (Figure 3-13); the late time plateau signal shows no effects for this run. Although this data set is incomplete, the basic results are similar to other observations. After the first several shots the OIII peak has increased by a factor of about 1.4 over its value in H_2. This increase can be explained by the difference in the mass of the working gas as would be consistent with the results of Section A. The smaller increase during the first several shots is probably due to the increase in the ratio of D to H in the very early ($\lesssim$ 200 μsec) plasma shown in Figure 3-10.

If desorption by the intrinsic impurities were dominant over desorption by hydrogen the oxygen effects would be small. The oxygen increase suggests that in an undoped Tokapole plasma, the working gas plays the major role in releasing light impurities. When the machine is dirty or heavily doped, the intrinsic impurities probably play a non-negligible role. More careful modeling of the time-dependence of the influx (Chapter 4) substantiates the conclusion that the plasma formed from the initial puff of working gas (and any dopant gas) has a strong interaction with the wall in the earliest stage of start-up.

Figure 3-13. OIII λ703 versus number of shots after switching the working gas to D_2, with one shot in H_2 after D_2 for a reference level.

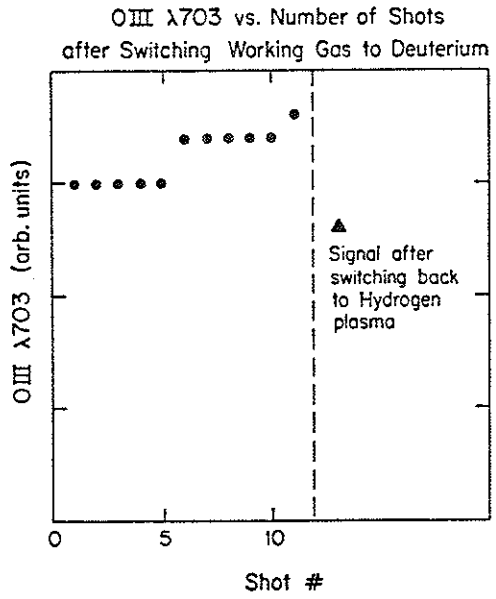

Figure 3-13

C. Intrinsic Impurity Doping Experiments

The understanding of doping experiments which use an intrinsic impurity as the dopant is complicated by the self-desorption process, especially at higher dopant concentrations. The observed impurity increase has two components: the increase of the dopant in the initially puffed working gas, which not only fills the vacuum chamber but also gets pumped by the walls before the discharge starts, and the additional wall impurity desorbed by the higher mass (doped) working gas. (Wall pumping of the dopant from the previous shot has been minimized for all of the data of this thesis by ensuring that the impurity concentration returns to its original level on the first shot after the data run.)

Intrinsic impurity doping has been a useful technique in tokamaks for measuring the absolute impurity concentration in the wall.[3,9] For low dopant concentrations the increase of oxygen with oxygen doping, for example, is linear. The extrapolation of the data points for each ion to zero intensity gives the O concentration in the undoped plasma. The technique may be modified for the effects of self-desorption as shown in Figure 3-14. The line through the data points for OIII λ703 versus doped O concentration has been extrapolated to give 2.0 X 10^{11} O atoms/cm^3. An estimate of the self-desorption is made from comparing data of similar mass impurities: NIII λ991 versus doped O and OIII λ703 versus doped Ne. Subtracting this line gives a corrected line which represents only O

Figure 3-14. Ionization peak signal versus dopant concentration. The X's are data points for OIII λ703 versus O doping through which a straight line (dotted) is drawn, ignoring the nonlinearity beginning at higher doping levels. The extrapolation back to zero doping signal indicates a concentration of 2 X 10^{11} cm^{-3}. A correction is made by subtracting the self-desorption, estimated from NIII λ991 versus O (dashed) and from OIII λ703 versus Ne (dotdashed). The corrected curve (solid) indicates a higher concentration of 2.5 X 10^{11} cm^{-3}.

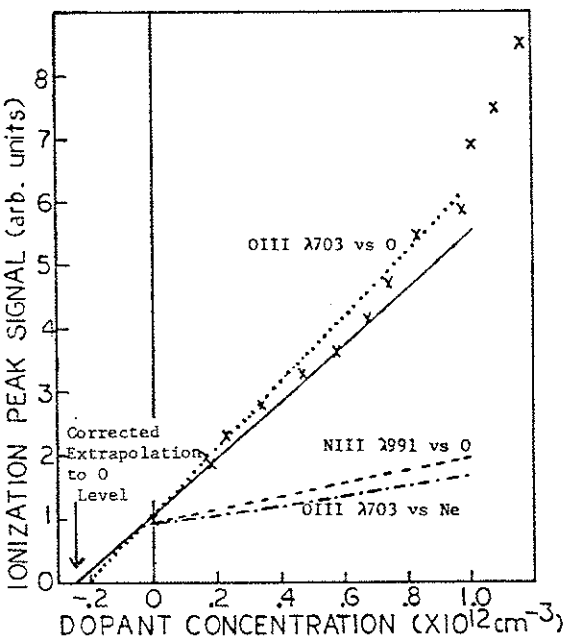

Figure 3-14

added directly to the plasma. This extrapolation gives a slightly higher value of 2.5 X 10^{11} O atoms/cm^3.

The nonlinear response of these experiments provides a useful comparison to the linear response of the experiments in Section A. Figure 3-15 shows the response of CIII, NIII, and OIII to O doping and of NIII and OIII to N doping. In Figure 3-15a the parabolic increase of OIII with doped O clearly occurs for a range of dopant concentration which is linear in NIII and CIII; however, for the same amount of doped N, OIII and NIII are both nonlinear (Figure 3-15b). Since the intrinsic O concentration is a factor of seven times higher than the N concentration, the difference in the nonlinearity must be the consequence of recycling during the discharge. These data are used for the model in Chapter 4 to quantify the recycling during start-up. Qualitatively one can already see in Figure 3-15a that the influx of light impurities must have a strong time dependence. If the plasma recycles several times, gaining effective mass from impurities with each encounter with the wall, all the doping series would be inherently parabolic. The linear response of O to exotic gas doping and the continued linearity of N and C during parabolic O response suggest an early decrease in the recycling rate. (Depletion of the surface contaminants may occur during a shot, but at Tokapole base pressures the Al walls will replenish the surface layer between shots.)

Figure 3-15. Comparisons of impurity response during intrinsic impurity doping, including high dopant concentration levels. The linear response of CIII λ977 and NIII λ991 versus O contrasts the nonlinear response of OIII λ703 versus O (Figure 3-15a) and of NIII λ991 and OIII λ703 versus N (Figure 3-15b).

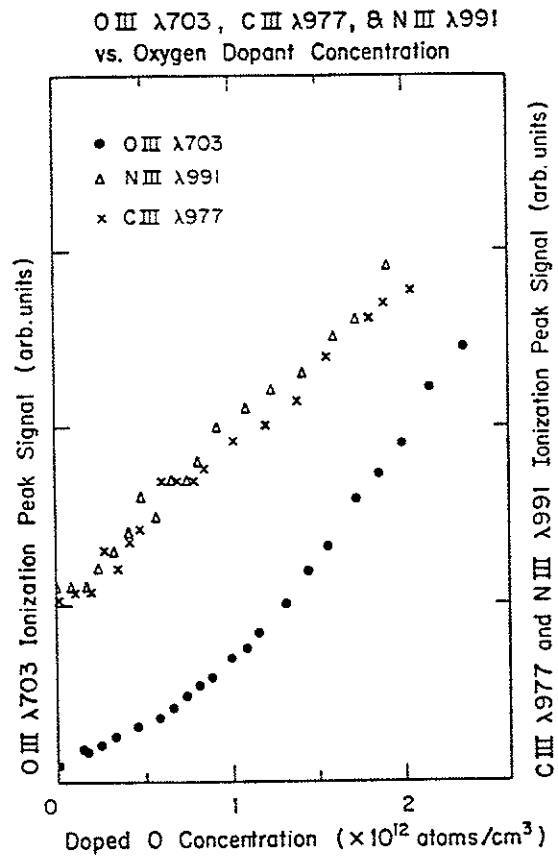

Figure 3-15a

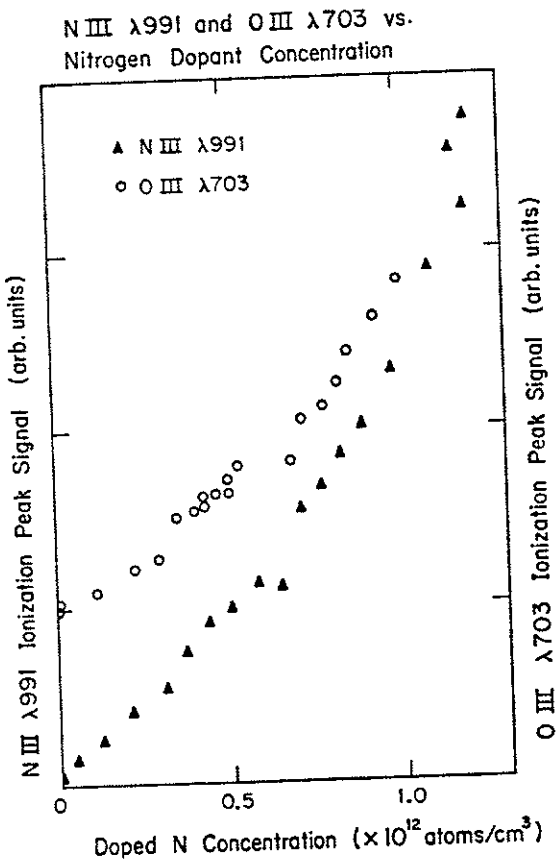

Figure 3-15b

For high enough dopant concentrations all low-Z impurity signals have a nonlinear response. Usually the gross plasma parameters begin to be affected as well, so that the experiments are difficult to interpret. Figure 3-16 shows the effects of high dopant concentrations for the same N data of Figure 3-15b. The parameter $\int I_p dt$ (amp-sec) is used as a figure of merit for the discharge. For the lower dopant levels the discharge length scales with $\int I_p dt$, so that I_p must be relatively constant. Here the increase in radiated power resulting from higher impurity levels probably slows the start-up process by consuming volt-sec. For higher dopant concentrations the current is lowered as well and the general plasma behavior deteriorates.

Figure 3-16. NIII λ991 and $\int I_p dt$ versus doped N concentration, showing the degradation of the plasma for high doping levels.

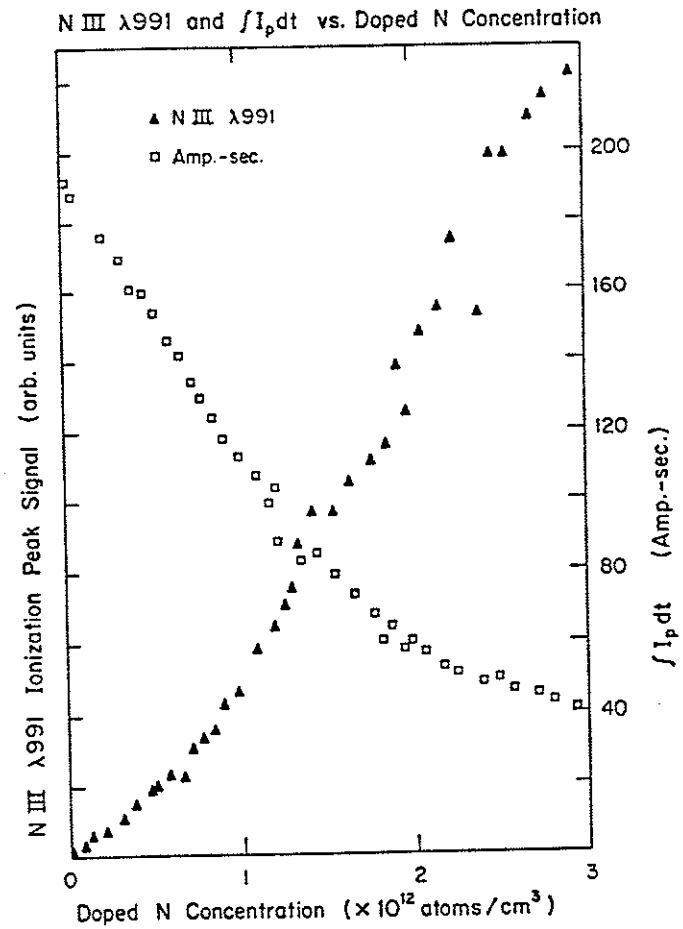

Figure 3-16

REFERENCES

[1]G. Lewin, Fundamentals of Vacuum Science and Technology, McGraw Hill, New York (1965).

[2]S. Dushman, Scientific Foundations of Vacuum Technique, 2nd ed., Wiley, New York (1962).

[3]R.J. Groebner, Ph. D. Thesis, University of Wisconsin (1979).

[4]G.M. McCracken, S.J. Fielding, S.K. Erents, A. Pospieszczyk, P.E. Stott, Nucl. Fusion 18 (1978) 35.

[5]S.J. Fielding and A.D. Sanderson, J. Nucl. Mater. 93/94 (1980) 220.

[6]H.C. Howe, J. Nucl. Mater. 93/94 (1980) 17.

[7]T.F.R. Group, J. Nucl. Mater. 111/112 (1982) 199.

[8]R.J. Groebner, University of Wisconsin Plasma Studies PLP 742 (1978).

[9]L. Oren and R.J. Taylor, Nucl. Fusion 17 (1977) 1143.

CHAPTER 4

ION-INDUCED DESORPTION DURING START-UP -- MODEL

A simple model of working gas and impurity recycling describes the major effects of the early-time doping experiments on Tokapole II. This model is consistent with the observed linearity of impurity increases with doping and the experimental observations of the time development of the oxygen series line radiation. The calculation uses a time-dependent coronal equilibrium rate equation for oxygen ionization and recombination[1,2] to find the influx term. A computer code solves for the emissivities of the ionizing oxygen states given $T_e(t)$, $n_e(t)$, the particle confinement time τ, all experimentally observable in principle, and an influx term, to be determined.

A. The Time-Dependent Coronal Model[2,3]

For a plasma in thermodynamic equilibrium, particle collision processes determine the population densities of the electrons in the various energy levels and in different ionic states. These population densities are given by the Boltzmann equation,

$$\frac{n_z^p}{n_z^q} = \frac{\omega_z^p}{\omega_z^q} \exp\left(\frac{\varepsilon^{p,q}}{kT_e}\right) \qquad (4\text{-}1)$$

and the Saha equation,

$$\frac{n_{z+1}^{g}\, n_e}{n_z^g} = \frac{\omega_{z+1}^{g}}{\omega_z^g}\, 2\left(\frac{2\pi m k T_e}{h^2}\right)^{3/2} \exp\left(\frac{\varepsilon_z^g}{kT_e}\right) , \qquad (4\text{-}2)$$

where n represents the population density for different energy levels p, q, and g (ground) and for different ionic states z and z+1, ω is the statistical weight of the designated level, ε is the energy difference between the levels, with ε_z^g representing the ionization potential of the ion of charge z from the ground level. The local thermal equilibrium model thus assumes a balance between the collisional excitation and ionization processes and their inverse processes. The atomic cross sections are not needed to determine the population densities.

For an optically thin plasma of low enough density, the probabilities of radiative transitions and collisional transitions are comparable, and thus the atomic physics must be taken into account. The steady-state phase of the tokamak's hot central core is fairly well described by the coronal model, which assumes a balance between ionization (and excitation) by electron collisions and radiative recombination (and decay). The plasma electrons are Maxwellian, and the population densities of the excited levels of an ion are negligible compared to the ground state density. For these processes,

$$n_e n_z^g\, S_z^g(T_e) = n_e n_{z+1}^g\, \alpha_{z+1}^g(T_e) \qquad (4\text{-}3)$$

and

$$n_e n_z^g\, Q_z^{g,p}(T_e) = n_z^p \sum_{q<p} A_z^{p,q} , \qquad (4\text{-}4)$$

where S is the ionization rate coefficient, α is the recombination rate coefficient, $Q_z^{g,p}$ is the electron excitation rate coefficient from g (ground) to level p, and $A_z^{p,q}$ is the transition probability for spontaneous emission from level p to level q, where q has a lower energy than p. The emission E of the line produced by a transition between levels p and q is given by

$$E_z^{p,q} = n_z^p\, A_z^{p,q} , \qquad (4\text{-}5)$$

where E is in units of photons/sec/cm^3.

For the start-up plasma, the temperature and densities are evolving so that the balance between ionization and recombination does not have time to equilibrate. A time-dependent coronal model may be used to replace Equation (4-3) to take account of ionization and recombination rates. The atomic lifetimes of the excited levels are much shorter than the relevant temperature evolution times so that Equations (4-4) and (4-5) are still applicable.

A computer program to calculate the oxygen ion population densities and emissivities for particular lines from the time-dependent coronal model has been written by R.J. Groebner. The plasma physics of start-up is included through an influx term Φ_0 and a set of particle loss terms, with confinement times τ. The equations are:

$$\frac{dn_0}{dt} = -S_0(T_e)n_e n_0 + \alpha_1(T_e)n_e n_1 - \frac{n_0}{\tau} + \Phi_0$$

$$\frac{dn_z}{dt} = -S_z(T_e)n_e n_z - \alpha_z(T_e)n_e n_z + S_{z-1}(T_e)n_e n_{z-1}$$

$$+ \alpha_{z+1}(T_e)n_e n_{z+1} - \frac{n_z}{\tau}$$

$$\frac{dn_{zL}}{dt} = -\alpha_{zL}(T_e)n_e n_{zL} + S_{zL-1}(T_e)n_{zL-1}n_e - \frac{n_{zL}}{\tau}, \qquad (4\text{-}6)$$

where n_z represents the density of oxygen of charge z, using OVII as the limit ion zL because of its high ionization potential (739.1 eV) relative to the plasma temperature. The rate coefficients used are discussed in Reference 2. Some additional processes are included to improve the accuracy, such as corrections for metastable levels. The overall accuracy of the calculation for volume-averaged T_e has been estimated to be within 50%, with the largest errors from uncertainties in the atomic rate coefficients.

B. Experimental Parameters Used in the Calculation

The computer code solves for the time-dependent emissivities of OIII λ703, OIV λ789, OV λ630, and OVI λ1032/1038, which are then compared to the observations made with the absolutely calibrated VUV monochromator. The best fit is determined when the predicted oxygen series lines match the experimental data, particularly for the ionization peak times and relative heights. With independent measurements of $n_e(t)$, $T_e(t)$, and τ to use in the calculation, the influx term can be varied until a best fit is found. In practice none of these quantities are well known but reasonable estimates can be made from the existing diagnostic measurements. The comparison of oxygen radiation with and without doping provides an additional check on these estimates.

The quantity $\bar{n}_e(t)$ is measured with the interferometer; however, this chordal integration is an inaccurate measurement of the central density during start-up. The interferometer views a large region of the common flux, where the density profile peaks early in time. The central density (and the volume-averaged density) might be expected to peak later in time with a larger value. These assumptions about the time-dependence of the density profile have been verified by profile measurements of the toroidal current density taken with a small Rogowski coil. The function $n_e(t)$ thus assumed for the simulation is shown in Figure 4-1.

Figure 4-1. n_e versus time used in the simulations.

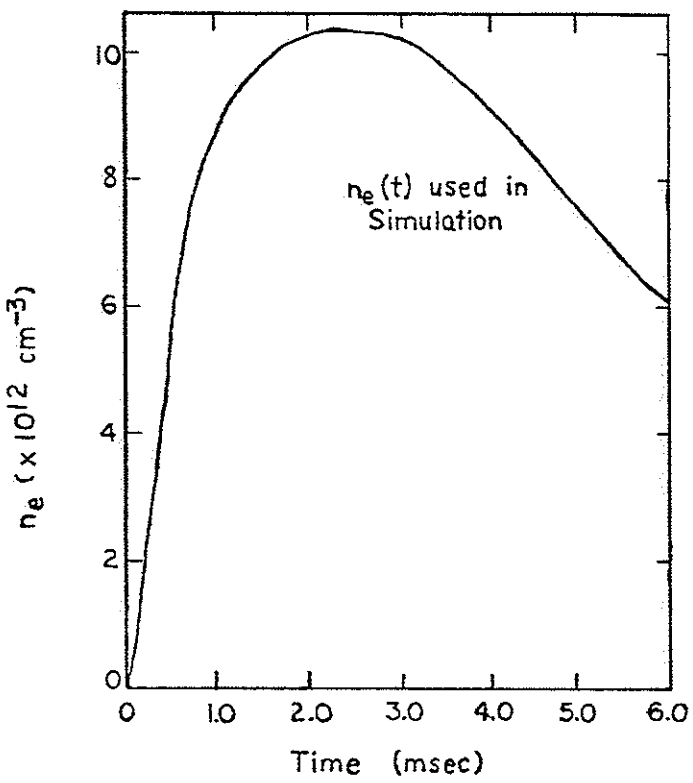

Figure 4-1

The values of τ and $T_e(t)$ are roughly estimated from the experiment, and then fit with the computer calculation. For the first step in the fitting process, one can arbitrarily assume that the influx term is zero, and that an initial concentration of 3×10^{11} cm^{-3} oxygen neutrals is uniformly distributed in the undoped plasma. The best particle confinement time τ found from these calculations is 1.0 msec for all oxygen states. Although this parameter is unknown experimentally, most tokamaks find that the particle confinement time is one to ten times the energy confinement time, which for Tokapole II is about 500 μsec. Fortunately, the calculation is not very sensitive to the value of τ used; the variation of τ between 500 μsec and 5 msec essentially does not affect the calculation for start-up. In principle each ionic state may have a different confinement time but this variation has also been found to have little effect on the calculation.

The times and heights of the ionization peaks in the calculation are extremely sensitive to the function $T_e(t)$. For this reason the procedure used here provides one of the best measurements of the volume-averaged $T_e(t)$ for the start-up phase of a tokamak. The function $T_e(t)$ which best fits the data is shown in Figure 4-2. The flatness of this function before 1.0 msec and the fast rise to maximum T_e are necessary features for matching the ionization peak times. For the first 1.0 msec a variation in T_e of a few eV makes a good fit impossible. During the time between 0.5 msec and 1.0 msec, T_e is clamped to a constant value by radiated power losses. The

Figure 4-2. T_e versus time used in the simulations.

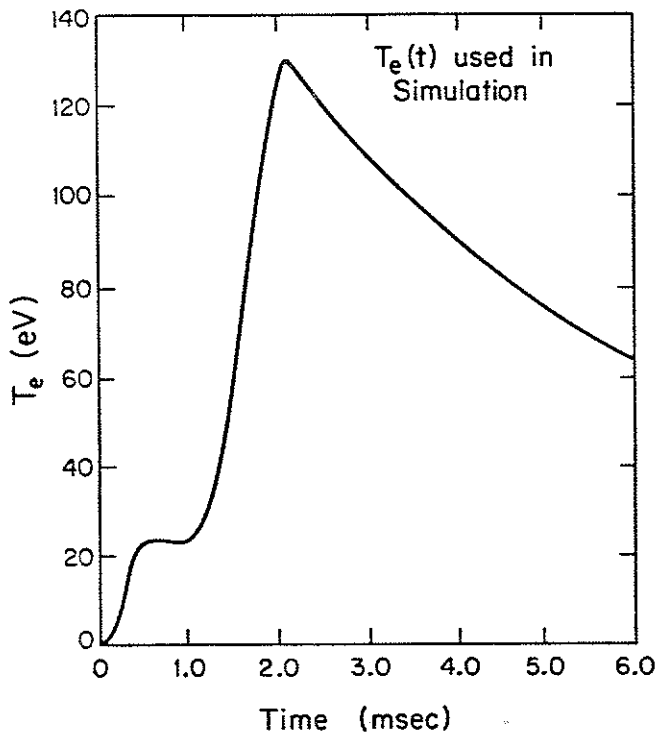

Figure 4-2

radiation barrier (at T_e of about 20 eV for a discharge with low-Z impurities[4]) is a maximum of low-Z radiation versus T_e, and must be overcome in order to ionize OIII. The time of the peak T_e is assumed to agree with the SXR peak time. The calculation is less sensitive to the magnitude of T_e between 1.0 msec and the time of peak T_e. The value of 130 eV agrees well with estimates from the measured conductivity T_e (and Z_{eff}). The oxygen series data and the simulated fit are shown in Figure 4-3 for the undoped case.

This calculation is also used to check the assumption that T_e does not vary during a doping series. For the data of Figure 4-4a the calculation is repeated, using the known initial oxygen density increase, and varying only $T_e(t)$. (This Figure represents the maximum dopant concentration for which the plasma characteristics are assumed not to change.) The function $T_e(t)$ calculated in this way has been shown in Figure 3-6. The difference between the maximum T_e of 130 eV and 100 eV should represent the major effect of doping on T_e. Up until 1.0 msec no effects on T_e are observed. Presumably the added oxygen keeps the plasma below the radiation barrier longer, and thus prevents the efficient use of the ohmic heating input power. For all the calculations shown in this chapter, the same function $T_e(t)$ is used; however, many variations of $T_e(t)$ for different influx functions have been made. The changes in the relative magnitudes of the oxygen series with doping are in the same direction as the T_e decrease, so that the 30 eV difference is an upper limit on the effect of doping on T_e. The simulated

Figure 4-3a. Emission of oxygen series line radiation (OIII λ703, OIV λ790, OV λ630, OVI λ1036) versus time for an undoped plasma case. The emission data are relatively calibrated and corrected for multiplet levels for OIV λ790 and OVI λ1032/1036.

Figure 4-3b. Simulation of emission of oxygen series line radiation versus time for the undoped plasma case.

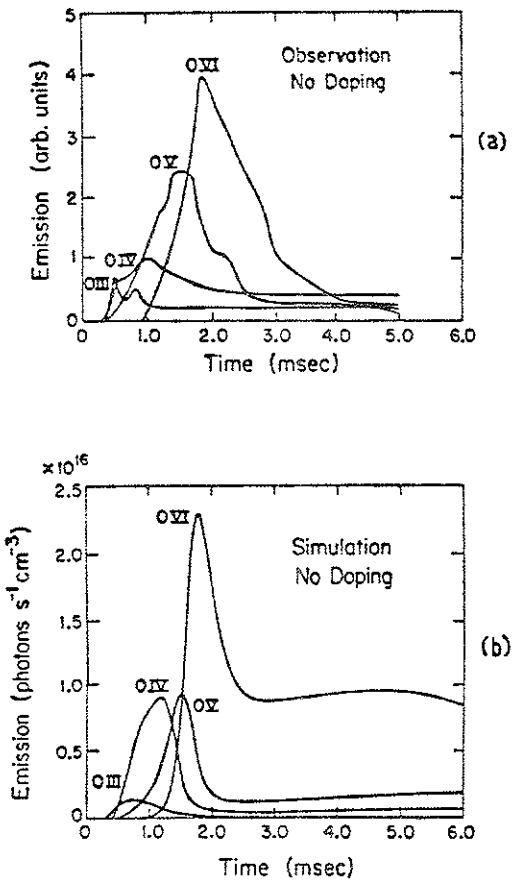

Figure 4-3

Figure 4-4a. Emission of oxygen series line radiation versus time for a plasma doped with oxygen. The simulations past 2.5 msec are not expected to match the data.

Figure 4-4b. Simulation of emission of oxygen series line radiation versus time for a plasma doped with oxygen. Note the fit to the data of Figure 4-4a is somewhat worse than for the undoped plasma case due to changes in the plasma parameters.

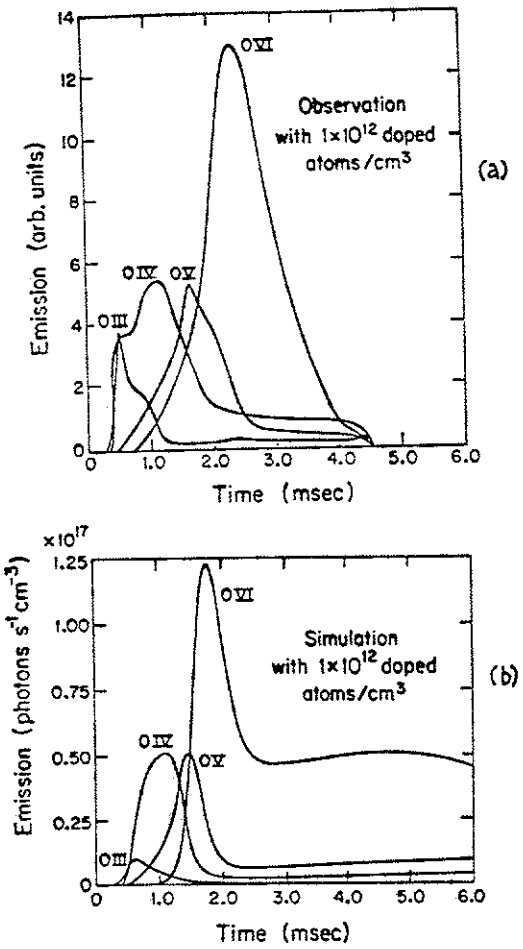

Figure 4-4

oxygen series for the doped case with the $T_e(t)$ of Figure 4-2 is shown in Figure 4-4b.

The overall accuracy of the T_e calculation has been estimated to be within 50%. In addition to the uncertainties of the atomic coefficients discussed in Section A, the use of zero-dimensionality is of questionable validity. In Chapter 6 some profile data are shown to substantiate the assumption that the impurities are uniformly distributed at the time of their ionization peaks. Certainly by the plateau phase the various ionic states of oxygen have different profiles dependent on the T_e profile. For example, for OIII a plateau is established by 1.0 msec; the zero-dimensional calculation cannot be expected to match this plateau value for OIII past this time.

C. Model of the Oxygen Influx

Using the input parameters $n_e(t)$, $T_e(t)$, and τ from Section B the time-dependence of the oxygen influx term $\Phi(t)$ is now varied. The total number of oxygen particles in the system (wall plus plasma) is assumed to be fixed. The number in the wall is determined from extrapolating the oxygen doping curve to zero signal. The variation of $\Phi(t)$ shows that the influx must be limited to a short duration in order to avoid a large build-up of the oxygen concentration between the OIII and OVI peak times and therefore too large a prediction of the emission of the higher ionic states.

A model of the impurity influx may be constructed based upon ion-induced desorption. For recycling of intrinsic impurity i, the flux term may be written[5] as

$$\frac{dN_i}{dt} = (\beta - 1)\frac{N_i}{\tau_i} + \frac{N_i^{wall}}{A}\left(\Sigma_j \frac{\sigma_{ji} N_j}{\tau_j}\right) \qquad (4\text{-}7)$$

where N_i is the number of impurity particles in the plasma, N_i^{wall} is the number of impurity atoms in the wall, A is the wall area, the sum is over all species j in the plasma, and τ_j is the characteristic time for the recycling process. The coefficients β and σ_{ji} are the reflection coefficient for particle i and the cross section for particle j to knock particle i off the wall, respectively. A similar flux term exists for all plasma species including the working gas, so that N_i will initially increase in time as more particles come off the wall. Furthermore, increasing the number of a species N_j (as by doping) should cause a nonlinear increase in the total number of particles. These build-up processes can continue until the impurity concentration in the wall has been depleted ($N_i^{wall} \to 0$), or until equilibrium is reached ($dN_i/dt \to 0$). Any time-dependence of the quantities τ_j or σ_{ji} could also limit the build-up. (For example, since desorption depends on the incident ion energy, the cross section σ_{ji} may be effectively time-dependent if a sheath potential is the source of the ion energy.)

For the computer calculation of the oxygen density build-up, Equation (4-7) is simplified to include desorption induced only by three species: protons p, oxygen ions X, and dopant ions D (which may be either exotic or oxygen). Since a reflected ion cannot be distinguished experimentally from a desorbed atom or ion of the same species, the coefficient β is lumped with the effective cross section σ. The confinement times are assumed to be the same for all species. The influx is assumed to be in the form of neutrals so that for Φ_0 of Equation (4-6), one has

$$\Phi_0 = \frac{N_X^{wall}}{A\,\tau}\left(\sigma_{pX} n_p + \sum_{z=1}^{zL}\left(\sigma_{XX} n_z + \sigma_{DX} n_z^D\right)\right) \qquad (4\text{-}8)$$

In order to keep the influx low after about 1.0 msec, only the low ionization states are kept in the sum. Keeping higher ionization states causes a small increase in the OVI emission. The further assumption that the cross sections are proportional to the ion mass gives the ratio of the cross sections. The determination of the influx for the undoped case is thus a calculation of σ_{pX}/τ. For $\sigma_{pX}/\tau = 4\times10^{-13}$ cm^2/msec (and, therefore, $\sigma_{XX}/\tau = 6\times10^{-12}$ cm^2/msec), the time-dependence of Φ_0 and the total oxygen concentration are shown in Figure 4-5. Figures 4-3 and 4-5 represent the best fit to the data for the undoped case.

Figure 4-5. Simulation of oxygen influx and total oxygen density versus time for an undoped plasma case. This case is the best fit to the data.

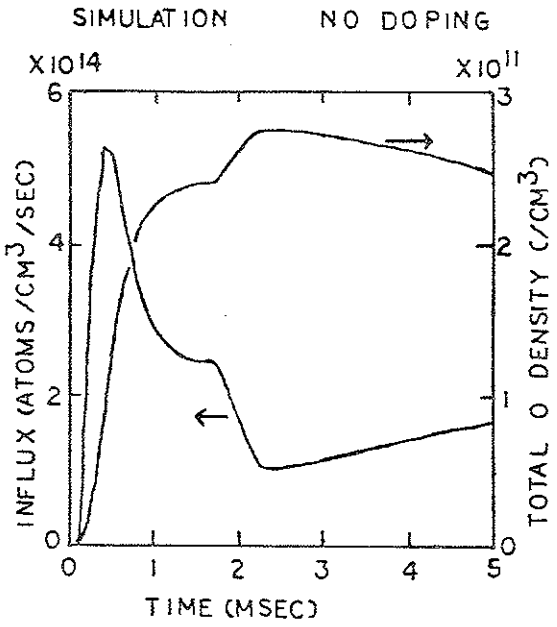

Figure 4-5

From the exotic gas doping experiments we have assumed the relative magnitude of σ_{DX}/σ_{pX}. The nonlinearity of the oxygen radiation increase with oxygen doping can be seen as resulting from the time-dependence of the n_z terms. (At any given time, the oxygen influx depends linearly on the ion densities.) The simulated increase of OIII with O doping is shown in Figure 4-6 for the above cross section values. This best fit curve for OIII versus doped O concentration begins to turn over at high dopant concentrations as the wall oxygen is eventually depleted. The data shown for such high dopant concentrations probably include effects on such plasma parameters as T_e; no fit can be expected.

In summary, the influx term based on the recycling model is found to be consistent with the early generation of oxygen. The quantity σ_{pX}/τ may be varied to fit the oxygen radiation. This quantity is then constrained to be within an order of magnitude for any reasonable fit to the data. Using the mass proportionality of the cross section, one gets a good fit to the nonlinear oxygen doping curve, which provides a consistency check on the time-dependence of Φ_0.

D. Discussion of the Influx Model and Desorption

An obvious constraint on the influx term for Tokapole II is that the wall impurity concentration not be depleted by 1.0 msec for an undoped plasma, since doping with an exotic gas increases the O concentration. The simulation of total oxygen concentration versus

Figure 4-6. Observation and simulation of OIII λ703 versus doped oxygen concentration for the best fit to the data. The data and simulations for the oxygen series versus time of Figures 4-3 and 4-4 are represented on this plot.

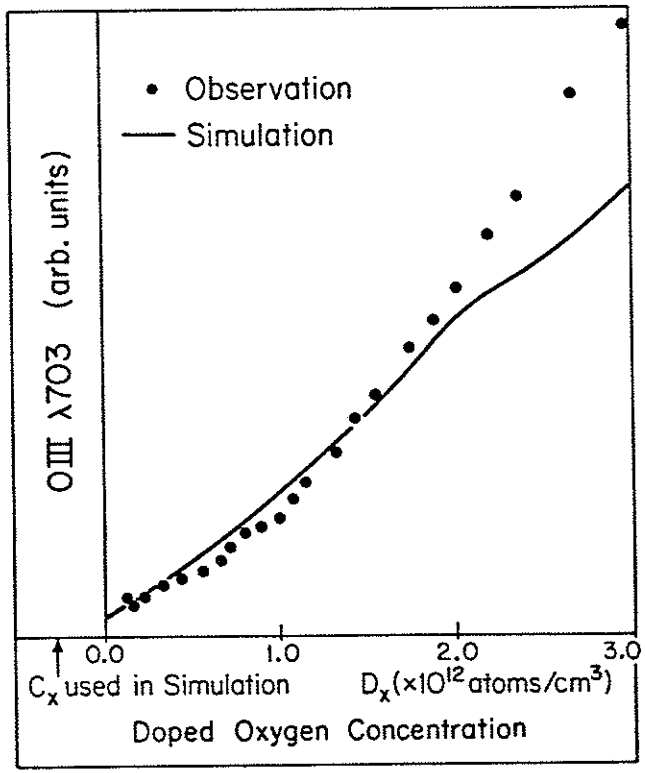

Figure 4-6

time of Figure 4-5 indicates that 80% of the oxygen to be desorbed is in the plasma by 1.0 msec and that the total wall concentration is never quite depleted during the start-up. Since the influx is strongest before this time, one might expect the proton term to dominate the oxygen term. At 0.5 msec the calculation gives $\sigma_{pX}n_p/\sigma_{XX}n_X = 4$. Since an order of magnitude increase in the impurity concentration with doping reverses the dominant term, one might expect a difference in the time-dependences of Φ_0 and the total oxygen concentrations. Indeed the early peak in Φ_0 is more pronounced and the wall oxygen is depleted sooner in the more heavily doped cases. These effects are somewhat subtle in the best fit case.

In order to illustrate the competition between the proton and the dopant term in the oxygen production, a simulation of OIII versus dopant is made (shown in Figure 4-7). The simulation curve through labeled points a and c represents OIII versus doped O; the curve through the labled points a and b represents OIII versus doped N. These simulation curves use cross sections a factor of 4 smaller than the best fit case, exaggerating the effect of this competition. Also shown in Figure 4-7 are OIII data taken during O and N doping on the same day. The OIII versus O data are the same as in Figure 4-6. The turn-over in the data for OIII versus N may be consistent with the depletion of wall oxygen by 0.5 msec, although the experimental reproducibility may be questionable. The simulations of time-dependence of the influx and the total oxygen

Figure 4-7. Observations and simulations of OIII λ703 versus O and N. These simulation curves do not represent the best fit to the data. Labeled points a and c fall on the simulation curve for OIII versus doped O. Labeled points a and b fall on the simulation curve for OIII versus doped N. These points are referred to in Figure 4-8.

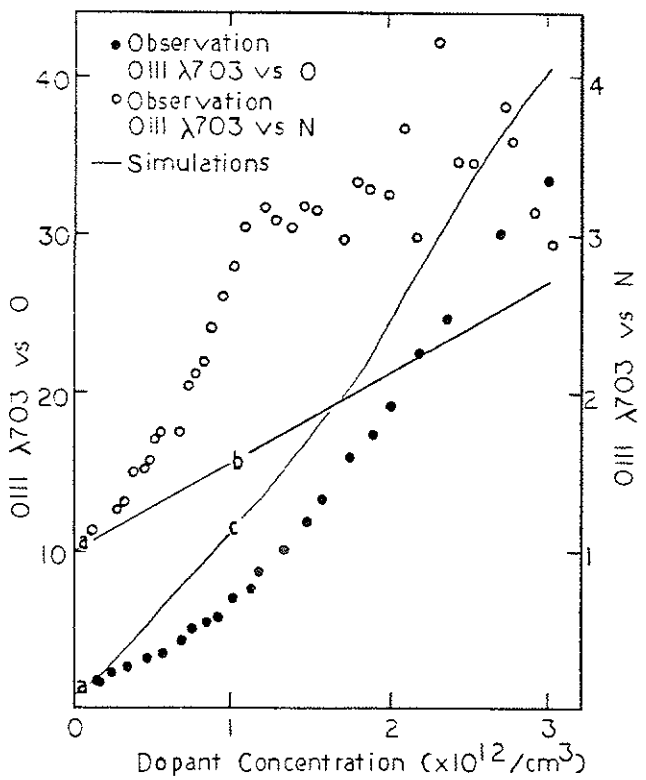

Figure 4-7

density (Figure 4-8) illustrate the differences between an undoped case (Figure 4-8a), OIII with N doping (Figure 4-8b), and OIII with O doping (Figure 4-8c). A larger value of n_X early in time produces a more rapid depletion of the wall oxygen, and thus a faster oxygen build-up in the plasma.

Thus the rate at which oxygen builds up early in the discharge determines the curve for OIII versus doped O. The factor of 4 difference in the magnitude of σ/τ between the simulations of OIII versus O in Figures 4-6 and 4-7 has changed this rate of build-up significantly. For the undoped Tokapole plasma then, the competition between the terms $\sigma_{pX}n_p$ and $\sigma_{XX}n_X$ and the time-dependence of N_X^{wall} in Equation (4-8) put tight constraints on the value of σ/τ (overall to within an order of magnitude).

The cross section estimates above imply effective desorption yields of the order 10^3 to 10^4 atoms per ion per msec. For an early-time τ the same as the particle confinement time of $\tau = 1.0$ msec, these yields seem large but possible for ungettered Tokapole II wall conditions[6]; however, the time scale of the recycling process responsible for the impurities in the central current channel must actually be quite short. A yield of 10 to 100 atoms per ion, thus implying $\tau \approx 10$ μsec, might be consistent with the data for ion-induced desorption and the poor confinement early in the discharge.

Figure 4-8. Simulations of oxygen influx and total oxygen density versus time for (a) the undoped case of Figure 4-7, (b) the nitrogen doped case of Figure 4-7, and (c) the oxygen doped case of Figure 4-7.

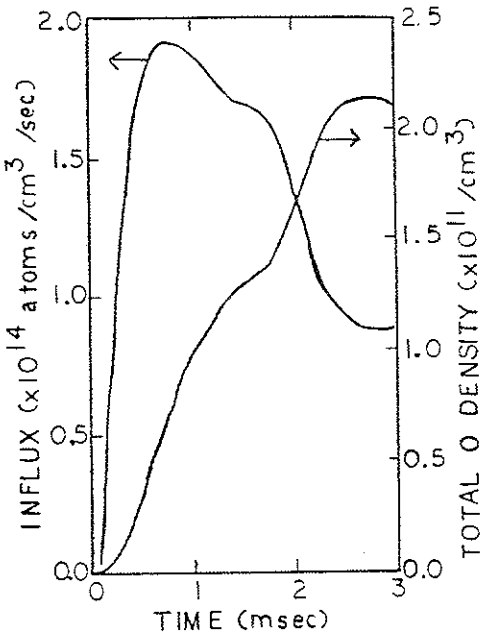

Figure 4-8a

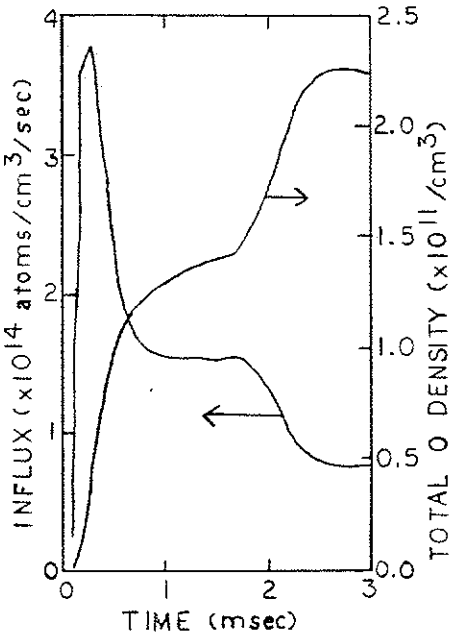

Figure 4-8b

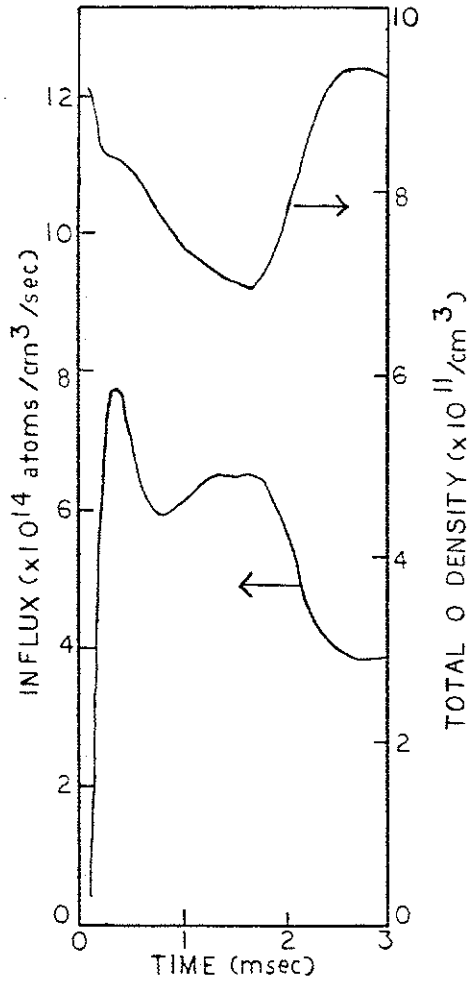

Figure 4-8c

Desorption by energetic ions and neutrals has been reviewed by McCracken and Stott.[5] Like sputtering, the desorption process transfers momentum from the incident particle to the surface impurity; however, the depletion of the surface layer can occur so that, unlike sputtering, the desorption rate is proportional to the surface concentration. For surface concentrations larger than one monolayer, the binding energy per molecule decreases so that the surface binding energy must then be taken into account. For Tokapole II the low-Z impurity concentration in the plasma implies a surface concentration of roughly one monolayer. (Gettered machines assume 0.1 monolayer.[7]) A recent compilation of desorption data[8] shows that the yields are generally in the range of 1 to 10 atoms per incident ion with very little difference seen for various metals, although cleaning techniques do decrease the yields. The energy and mass dependence has been studied for these cases and modeled effectively for energies above 100 eV.[9,10,11] For low energies, contributions from the bombarding, or primary, ion and from the backscattered primary ion are important. For Tokapole II, doping has never increased the aluminum impurity concentrations, so that the energy of the primary ion might be expected to be less than the sputtering threshold of about 100 eV. The threshold for desorption is much lower, on the order of 30 eV. Data which are representative of the energy dependence of desorption cross sections for rare gas ions are shown in Figure 4-9.[8,9] With some exceptions for certain adsorbed gases, the desorbed species is usually released

Figure 4-9. Desorption cross section versus incident ion energy. These data are taken from a compilation of all desorption data by Sagara and Kamada and include all measurements with data points below 100 eV. Note that the only such data are from Winters and Sigmund, for desorbing nitrogen from tungsten with perpendicular beams of He^+, Ne^+, Ar^+, Kr^+, and Xe^+.

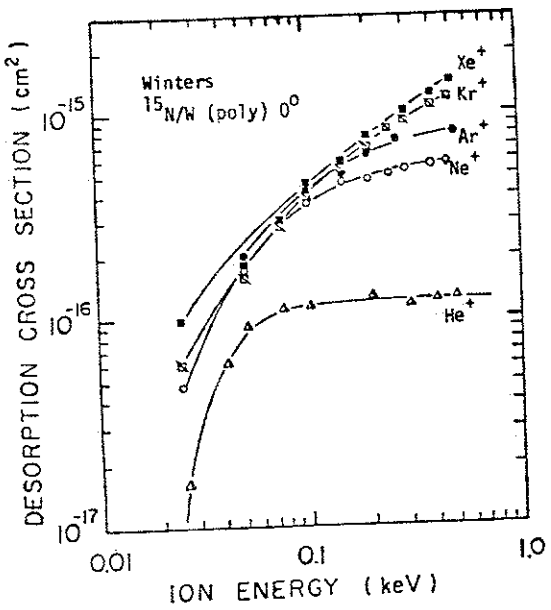

Figure 4-9

in the form of neutral atoms. For proton bombardment or for the larger yields the momentum transfer implies released atoms of very low energy. Thus the influx model used here is consistent with other desorption studies. The possible effects of doped impurities on the sheath potential, i.e. the bombardment energy, or on the particle confinement time are not considered in the model, since they seem to be unphysical. A variation in the average charge state of the bombarding species must certainly occur between He and Ar, so that some of the gas dependence may be due to energy rather than mass; without a measurement of the bombarding energy the importance of this effect cannot be determined, and therefore is not included.

The transition from start-up to the plateau with spatially ordered ionization states for oxygen seems to start quite early in the discharge. The OIII λ703 plateau has reached its steady-state value by 1.0 msec, so that edge recycling must be essentially isolated from the center by this time. Hints of edge recycling contributing to the impurity content of Tokapole II plasmas after the large initial influx are seen in the small increase of the plateau level of impurity signals with early-time doping. By the time the plasma is hot enough to lose energetic particles to the wall, the shielding of the center is in effect. This claim is consistent with the experience of several tokamaks with titanium gettering. The reduction of early impurity concentrations with gettering may be as much as an order of magnitude without reducing

the plateau concentrations.[12] Experiments of this nature on Tokapole II are discussed in Chapter 6.

In conclusion a momentum transfer process is responsible for the early-time light impurity levels in Tokapole II, with the cross-section for desorption proportional to the mass of the incident ion. The observation of linear increases of impurities with doping simplifies the influx term in the model to include mostly the initially puffed hydrogen and dopant.

REFERENCES

[1]Equipe T.F.R., Nucl. Fusion 15 (1975) 1053.

[2]R.J. Groebner, University of Wisconsin Ph.D. Thesis (1979).

[3]R.W.P. McWhirter, "Spectral Intensities" in: Plasma Diagnostic Techniques, ed. by Richard H. Huddlestone and Stanley L. Leonard, Academic Press, New York (1965) 201.

[4]C. Breton, C. de Michelis, and M. Mattioli, Nucl. Fusion 16 (1976) 891.

[5]G.M. McCracken and P.E. Stott, Nucl. Fusion 19 (1979) 889.

[6]S.K. Erents and G.M. McCracken, in: Atomic Collisions in Solids, Vol. 2, ed. by S. Datz, B.R. Appleton, C.D. Moak, Plenum Press, New York (1975) 625.

[7]S.J. Fielding and A.D. Sanderson, J. Nucl. Mater. 93/94 (1980) 220.

[8]A. Sagara and K. Kamada, J. Nucl. Mater. 111/112 (1982) 812.

[9]H.F. Winters and P.J. Sigmund, J. Appl. Phys. 45 (1974) 4760.

[10]E. Taglauer and W.J. Heiland, J. Nucl. Mater. 76/77 (1978) 328.

[11]M.T. Robinson and I.M. Torrens, Phys. Rev. 93 (1974) 5008.

[12]R.J. Taylor, R.F. Bunshah, and F. Schwirzke, J. Nucl. Mater. 93/94 (1980) 338.

CHAPTER 5

PRODUCTION OF METAL IMPURITIES

The metal impurity concentrations in Tokapole II have not been measured, since relative comparisons cannot be made as they have been for gas dopants. Nevertheless, metal impurity contributions to the radiated power may be significant. In 1979 Groebner had attributed 40% of the radiated power to the unmeasured metal components.[1] Since then, the plasma quality has changed somewhat, in that probes are no longer useable in the central regions, even for plasma conditions that are the same in density and temperature. The assumption that the machine is "cleaner", based on observations that the low-Z impurity content has been reduced by the overnight glow discharge cleaning, has seemed reasonable; however, the discharge quality over the past years has been observed in isolation from other changes in running procedures only for the case of the low q discharges. For those plasmas, a definite change in the discharge quality has been observed although the temperature and density have been the same. Attempts to make the plasmas "dirtier" by adding impurity gases, biasing the rings, running after vacuum accidents, and running with known leaks have not successfully allowed the use of probes at the center.[2] Similarly "clean" conditions, including additional probe cleaning, have also not helped. Since the metal

impurities are not well understood in Tokapole II, they have become a prime target of speculation in reference to the discharge quality. Supporting evidence that their character may have changed in the discharge is found from observations that the walls are more heavily coated with copper, presumably from pulsed and glow discharge bombardment of the rings.

The effects of metal impurities in a plasma can be much more serious than the effects of low-Z impurities, both from their increased contribution to radiation and from their large contribution to the plasma resistivity. Figure 5-1 shows the radiated power for oxygen (Z=8), aluminum (Z=13), and copper (Z=29) in the range of Tokapole II temperatures, and the average charge for each of these impurities.[3] The relative contributions to radiated power in Tokapole II are demonstrated by considering a 1% concentration of oxygen and copper in the volume within the separatrix, at an electron density of 1×10^{13} cm^{-3}. At T_e = 30 eV oxygen radiates 3 kW, whereas copper radiates 7 kW; however, at T_e = 100 eV oxygen only radiates .03 kW, whereas copper radiates 30 kW. Groebner's conclusion that radiated power was less than 20% of the input power in 1979 (P_{in} = 200 kW) may not still be applicable since the input power is now lower, and the metal concentrations have not been monitored. Changes in standard procedures (particularly adding the damping resistor) have reduced the input power in recent years. Also during the late plateau, the current is generally lower than during the first few msec. Using

Figure 5-1. Calculations from the average ion model, used to simplify the equations for all ionization states in a coronal equilibrium. Agreement with other models is good for T_e above 100 eV and Z below 42.[3]

a. Radiated power versus T_e for oxygen (Z=8), aluminum (Z=13), and copper (Z=29).

b. Average charge versus T_e for oxygen, aluminum, and copper.

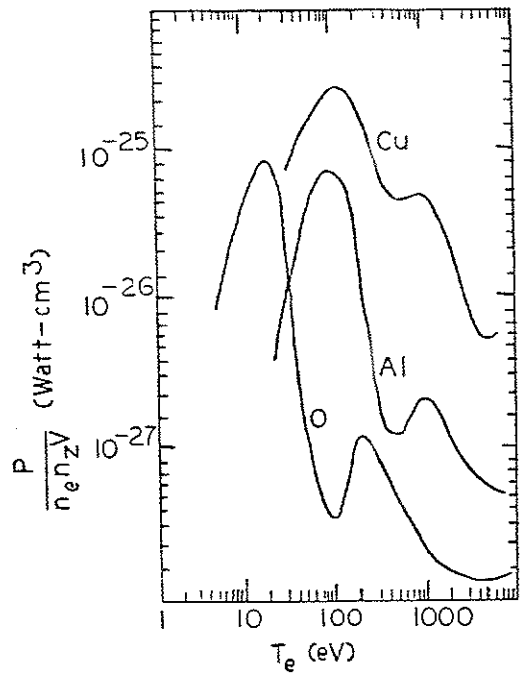

Figure 5-1a

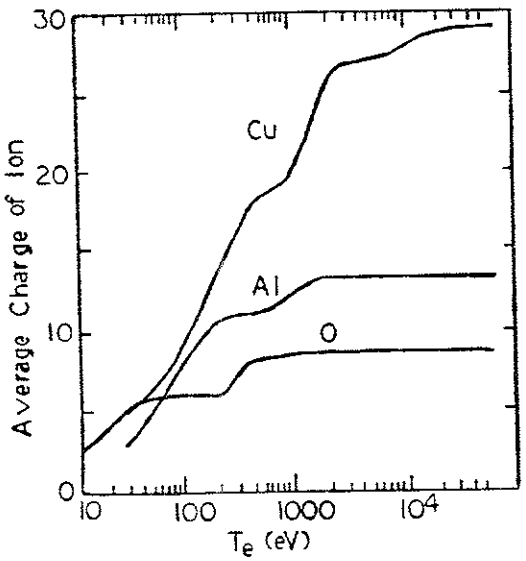

Figure 5-1b

the plateau values, I_p = 20 kA and $V_{loop} \approx 4$ V, gives P_{in} = 80 kW. Comparing Groebner's measurements of conductivity temperature and spectroscopic temperature implies a copper concentration (ignoring aluminum) of about 2%; comparing his radiated power measurements with the low-Z impurity contributions implies a copper concentration of 0.5% to 1%. Present estimates from T_e measurements are roughly similar. The speculation that the glow discharge procedure may have increased the copper concentration in the plasma since Groebner's measurements suggests that copper radiation may be a major power loss mechanism for the Tokapole II steady-state. Hollow T_e profiles have been measured in some tokamaks, particularly PLT, caused by high energy tungsten radiation in the ultrasoft xray region.[4] The VUV monitors used for general monitoring purposes would not observe a change in the copper radiation at 100 eV since they are limited to wavelengths above 400 A to 500 A, or to energies below 30 eV. Copper radiation from the plasma central region would be expected to radiate more of its energy between 100 A and 400 A. (Groebner's data include filter measurements of this region, and thus had taken this radiation into account in the power balance.[5])

In order to understand the production of metals in comparison to that of low-Z impurities, the effects of doping on metal line radiation have been observed. The remarkable result that AlIII λ3602 has never increased with doping limits the possible mechanisms. The implication is that during start-up the sheath potential must be below the sputtering threshold (for singly charged

ions). A reasonable estimate of this upper limit on the sheath potential is about 100 eV. Since sputtering increases with the incident ion density, and with the mass of the incident ion, sputtering is clearly not important during start-up.

Other tokamaks have reported that unipolar arcing is usually the dominant production mechanism for metals during start-up.[6,7,8] Experiments on JFT-2 have correlated runaway electron bursts with increases in the edge potential[7]; additionally, these potential spikes during start-up have been correlated with spikes on the molybdenum radiation from the wall.[6] During start-up the MHD instabilities associated with rational q surfaces produced during current build-up presumably cause losses of runaway electrons to the walls.[9] On Tokapole II arc tracks have been observed on both the walls and the rings; spikes in the edge potential have also been observed (Figure 5-2) but not correlated with either metal production or with runaway electrons.

The results of several experiments, including doping and ring biasing, demonstrate the difficulty of understanding the production of copper. In doping experiments, the radiation from CuI λ3247 increases with dopant concentration and with the mass of the dopant gas. Figure 5-3 illustrates these dependences. Unfortunately, the usefulness of CuI radiation as a monitor of copper concentration has not been demonstrated, since both its time-dependence and its low ionization energy differentiate it from the lines used for the low-Z impurities. (The identification of ionic copper lines is difficult,

Figure 5-2. Edge potential and AlIII λ3602 versus time. The floating potential is measured with a Langmuir probe located 2 cm from the wall. No correlations between edge potentials and aluminum production have been made yet for Tokapole II.

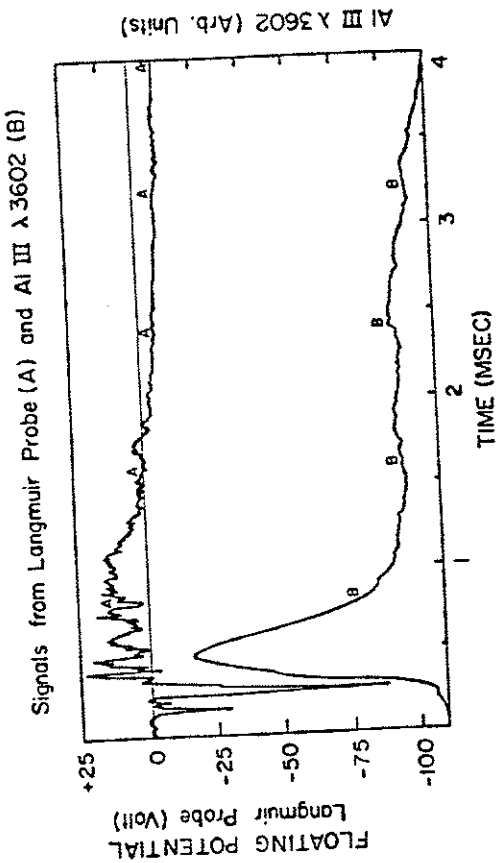

Figure 5-2

Figure 5-3. Relative increase of CuI λ3247 versus dopant mass. Sine no H doping data were taken during CuI observations, the increase is normalized to 4 for doped He. The error bars represent uncertainties in the slope for the few data points taken.

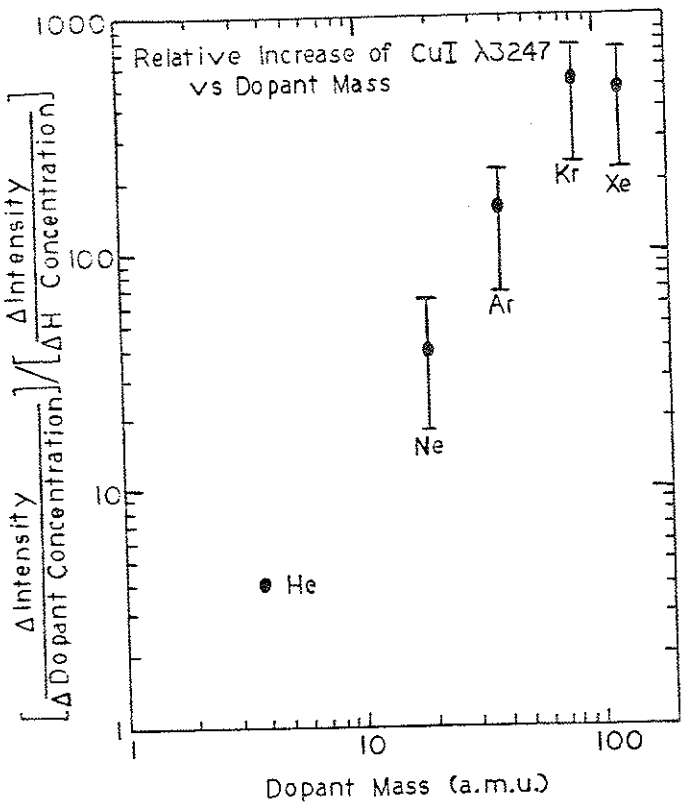

Figure 5-3

as suggested from the spectral line identification in Reference 1.) Nevertheless, one can qualitatively conclude that the copper production includes a term that depends on concentration and mass. Two processes are possible: sputtering of the rings and desorption of loosely-bound copper from the wall. A comparison of sputtering yields for copper and aluminum, made from the compilation of sputtering data in Reference 10, shows that for 100 eV incident ions the sputtering yield for copper is five times higher than for aluminum. Sputtering yields versus energy for aluminum, titanium, and copper using incident He are shown as an example in Figure 5-4.[11] Since the data of Figure 5-3 were taken before the start of overnight glow discharge cleaning, the desorption of copper from the walls might be expected to be larger now. Yields for ion-induced desorption of adsorbed residual gases are two to three orders of magnitude higher than sputtering yields for solid materials. Meanwhile, the observation of arc tracks suggests that unipolar arcing is also important for copper during the start-up. On a few occasions, SXR chords intersecting the line of sight of the ring support structures have shown large coherent spikes during start-up, possibly associated with runaway electrons bombarding the supports (Figure 5-5). Similar spikes have been observed on CuI λ3247 radiation from the ring region. CuI radiation often peaks later than AlII or OI, also suggesting a different source. Features observed on CuII λ2701 signals are consistent with this

Figure 5-4. Energy dependence of sputtering yields of aluminum, titanium, and copper for incident Helium ions. The solid curves are empirical fits to data from several authors. The dashed curves are theoretical.

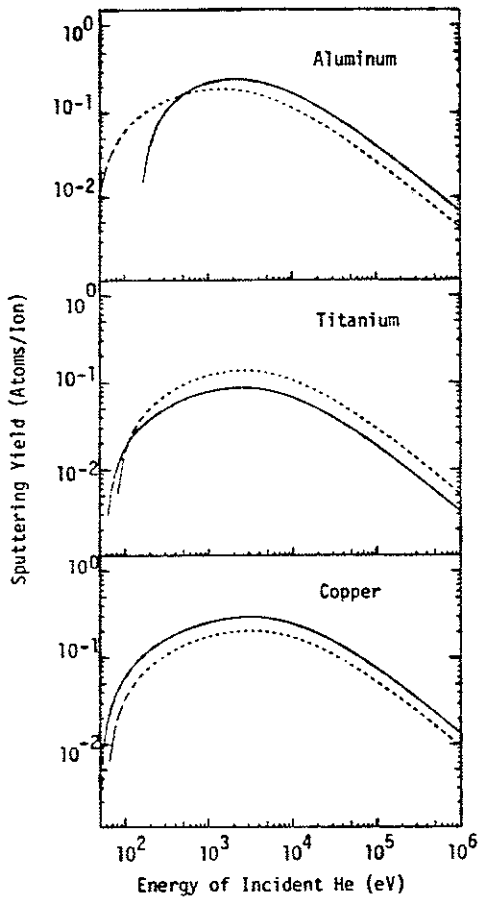

Figure 5-4

Figure 5-5. SXR chord at side 60° port versus time during start-up. These pictures are from different shots.

a. Chord intersecting line of sight of ring support (25° tilted up from center). It should be noted that very little signal is observed from the rings themselves (20° up from center), or from other toroidal angles (25° up at side 240°).

b. Central chord.

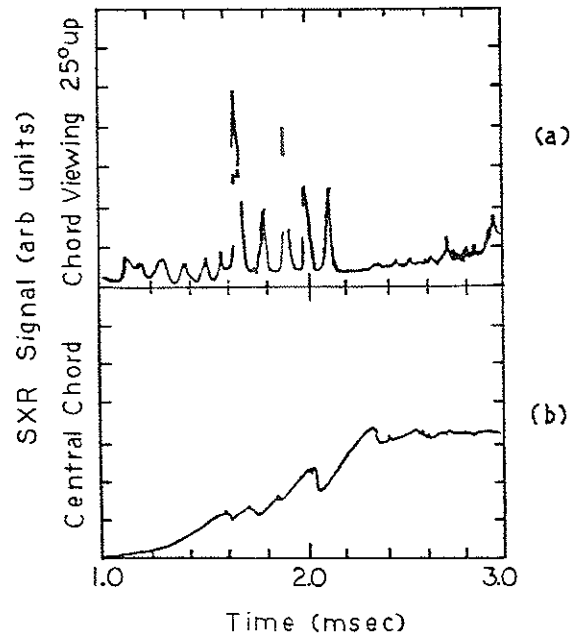

Figure 5-5

interpretation.[12] Probe and ring biasing experiments have been performed to aid the understanding of metal production.

Probe biasing experiments have consisted of placing a metal-tipped probe into the plasma, and comparing the effects of various bias voltages. In principle, an Al-tipped probe could be used to measure the metal content of plasma, similar to the low-Z measurements described in Chapter 3. An integrated measurement of Al radiation compared to a measurement of the mass lost from the tip during a single shot might provide the increase in Al concentration in the plasma; however, this technique is made more difficult by the presence of arcs. During the first several shots the probe tip has been observed photographically to exhibit unipolar arcing.[13] Only after several shots is the probe tip conditioned to allow consistent measurements.

Figure 5-6 shows a comparison for AlIII λ3602 along a line of sight a few cm from the tip between no applied voltage and a negative bias voltage. Figure 5-7 summarizes the probe biasing data. No trends are seen in the Ar doping, contrary to what might be expected from the mass dependence of sputtering. The bias has little effect during start-up. Perhaps the energy of ions at the center is too low to sputter the probe, or the wall is simply a larger source; however, the effects late in time imply that the probe can be a large source. The negative bias data suggest that during the plateau, highly stripped impurity ions have formed in the

Figure 5-6. AlIII λ3602 versus time with aluminum-tipped probe in the center of the plasma. The viewing chord is tilted a few degrees from the probe. The bias voltage is applied to the probe tip relative to the wall. A comparison between the signals for no applied voltage and for -100 volts is shown.

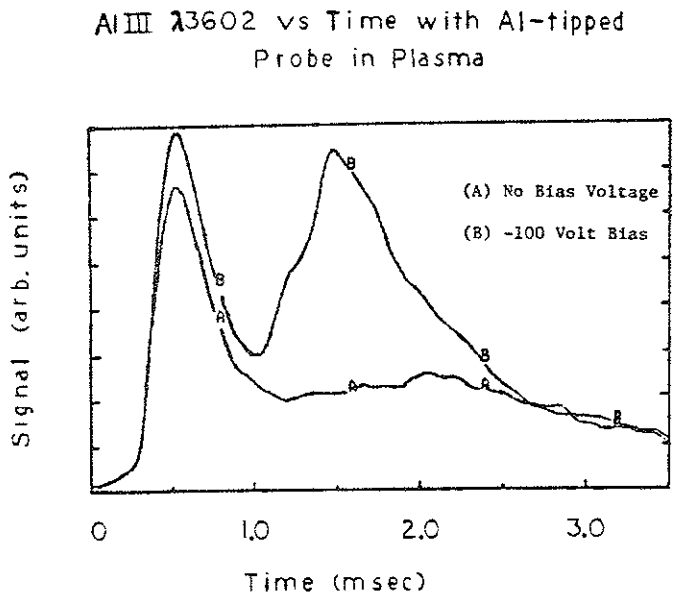

Figure 5-6

Figure 5-7. Relative change in AlIII λ3602 versus voltage applied to the probe described in Figure 5-5. Circles represent the signal at the ionization peak time (t=0.5 msec) and triangles represent the plateau signal increase (t=1.3 msec).

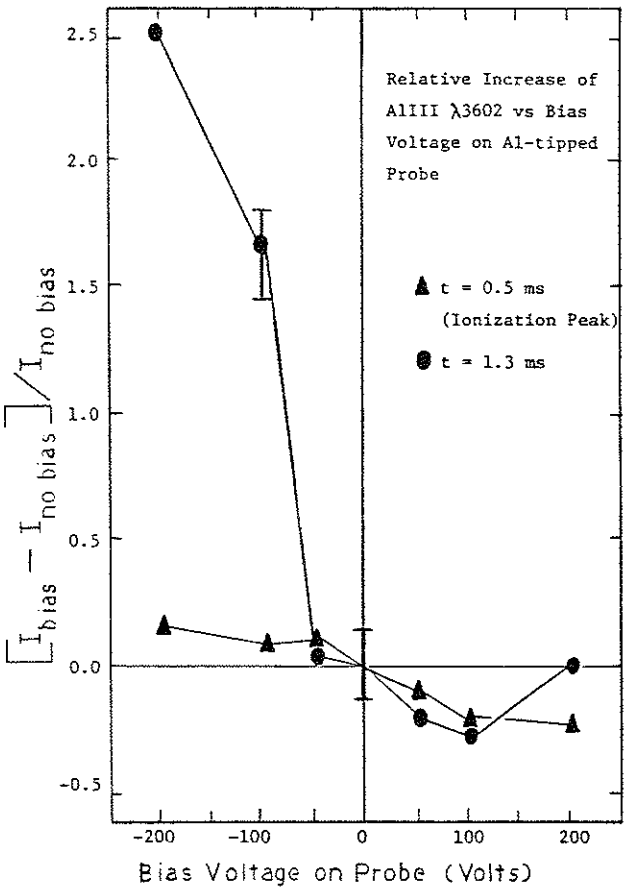

Figure 5-7

center so that the probe's sheath potential can accelerate them easily.

The ring biasing experiments may be seen as a continuation of experiments described in Reference 1. Large bias voltages of ±200 V can now be applied to the rings for the discharge duration. Figure 5-8 summarizes the new data, showing that the biasing effects on impurity concentrations are small. One explanation is that the rings are not large sources of impurities relative to the walls. The field lines around the rings may be quite effective in preventing particles from hitting the rings, although the ring supports would be expected to intersect the field lines. A second explanation is that the plasma adjusts itself to the appropriate voltage, since the bias voltage is applied between the rings and the wall. Groebner's Langmuir probe data taken in the scrape-off region during ring biasing suggests that the plasma potential changes with biasing.

In summary, a likely scenario for metal production in Tokapole II is that the walls may be a strong source of impurities, including copper, relative to the rings. Unipolar arcing is probably important during the start-up, with sputtering less important. No conclusions can be drawn for the plateau periods, except from the experience of other tokamaks, that sputtering dominates.[9] Experiments in which the electrons are added to make the plasma more negative with respect to the wall show that ion sputtering during steady-state decreases with decreasing sheath

Figure 5-8. Relative change in AlIII λ3602 (triangles), CuI λ3247 (circles), and OIII λ3760 (squares) versus ring bias voltage. The voltage is applied to all four rings relative to the wall for the duration of the discharge.

a. At t=0.7 msec, near the ionization peak time for AlIII.

b. At t=1.6 msec, during the plateau phase.

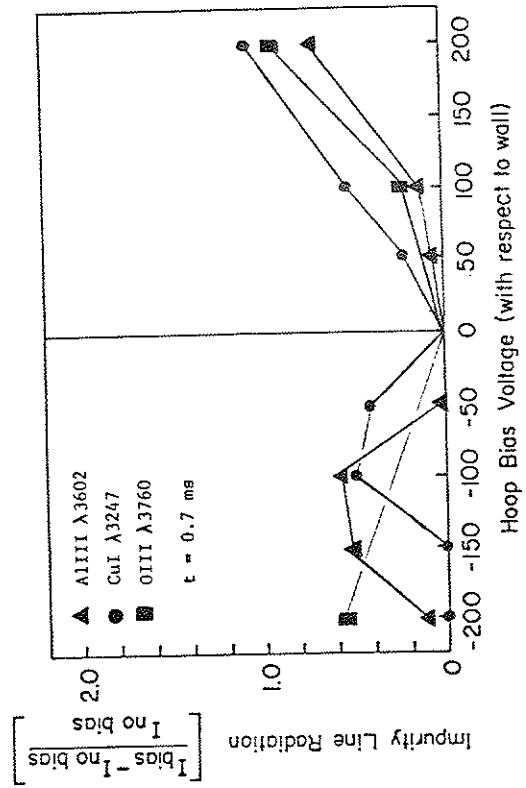

Figure 5-8a

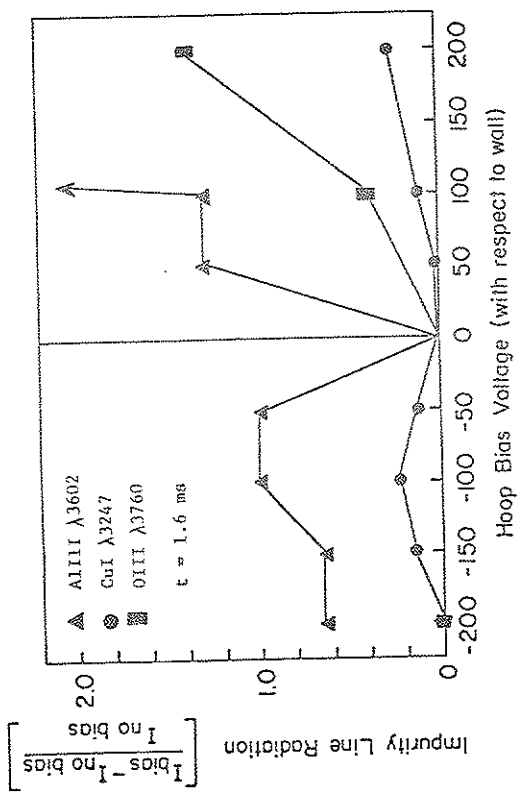

Figure 5-8b

potential.[14] The effects of glow discharge cleaning on the copper population in the plasma may be quite deleterious. Originally the glow voltage on the rings was high enough to cause electron sputtering. With the lower voltage on the rings used now, the glow sputtering of copper should be reduced to a tolerable level, but the resulting reduction in copper in the plasma may not occur without a major effort to clean the copper from the walls. Because copper radiation can be a large power loss mechanism if the copper concentration is a few percent, the reduction of copper may be important for raising the electron temperature. Ring supports may be protected by a less sputterable material. The use of heavy gettering may also reduce the loosely-bound copper on the wall surface. Plans are being made to implement some of these suggestions.

REFERENCES

[1] R.J. Groebner, Ph.D. thesis, University of Wisconsin (1979).

[2] T.H. Osborne, private communication.

[3] D.E. Post, R.V. Jensen, C.B. Tartar, W.H. Grasberger, and W.A. Lokke, Atomic Data and Nucl. Data Tables 20 (1977), 397.

[4] V.Arunasalam, et al., Proc. 8th European Conf. on Controlled Fusion and Plasma Physics, Prague, Vol. II, (1977) 17.

[5] R.J. Groebner and R.N. Dexter, University of Wisconsin Plasma Studies PLP 807 (1979).

[6] D.E.J. Goodall and G.M. McCracken, Nucl. Fusion 19 (1979) 1396.

[7] M.Maeno, H. Ohtsuka, S. Yamamoto, T. Yamamoto, N. Suzuki, N. Fujisawa, and N. Ogiwara, Nucl. Fusion 20 (1980) 1415.

[8] H. Ohtska, M. Maeno, N. Suzuki, S. Konoshima, S. Yamamoto, and N. Ogiwara, Nucl. Fusion 22 (1982) 823.

[9] G.M. McCracken, J. Nucl. Mater. 93/94 (1980) 3.

[10] H.H. Anderson and H.L. Bay in: Topics in Applied Physics, Vol.47, Sputtering by Particle Bombardment I, R. Behrisch, ed., Springer-Verlag, New York (1981).

[11] N. Matsunami, Y. Yamamura, Y. Itikawa, N. Itoh, Y. Kazumata, S. Miyagawa, K. Morita, and R. Shimizu, Nagoya University, Japan, Institute of Plasma Physics Report IPPJ-AM-14 (1980).

[12] R.N. Dexter, private communication.

[13] N.S. Brickhouse, University of Wisconsin Plasma Studies PLP 868 (1982).

[14] R.J. Taylor and Lena Oren, Phys. Rev. Letts. 42 (1979) 446.

CHAPTER 6

IMPURITY EVOLUTION DURING START-UP

The preceding chapters have identified ion-induced desorption as the major production mechanism for the low-Z impurities during start-up. This description implies specific characteristics of the edge plasma, which must also be consistent with the information on metal impurity release. Measurements of edge parameters during start-up are included in this chapter. In the oxygen influx model, the oxygen ions are assumed to be uniformly distributed prior to their ionization to the next state. Although the degree of localization of the source of oxygen (the entire wall versus a local hot spot near a puff port or obstruction) is difficult to discern for the earliest times, oxygen profile information is available by about 200 usec from OIII λ3763. The data shown in this chapter are preliminary in the sense that much more profile information is needed to model either the edge plasma or the transition from uniform impurity distribution to recycling or accumulation. The intentions here are simply to present the data and to indicate the types of information one might extract from them. The probe measurements in particular are notoriously unreliable for rapidly changing conditions.

Although the start-up method is thought to affect the early impurity concentrations, the best method for avoiding impurity release from the walls is usually empirically derived for each machine. The degree of MHD activity during the current ramp phase probably determines the amount of release of impurities by unipolar arcing; various machines program the start-up for either slow or rapid current build-up.[1] ECRH preionization has been reported to reduce impurity levels[2,3]; however, more recent experiments on Tokapole II suggest that many parameters change with the impurity concentrations. Isolating the changes in impurity levels from other interrelated effects may not be possible. On Tokapole II applying a small d.c. vertical field and titanium gettering also alter the impurity levels. More detailed studies of edge parameters and impurity profiles during various start-up procedures are being conducted.[4]

A. Edge Parameters

Probe measurements of edge parameters during start-up are discussed in this section. The magnitudes of the time-averaged electric potential and electron temperature are consistent with the observed desorption of oxygen. The time-dependent signals include spikes suggestive of unipolar arcing.

The probes used to measure V_f (the floating potential) and T_e on a single shot are three-tipped Langmuir probes.[5] A permanent diagnostic probe exists in the bridge region on the vacuum field

separatrix. A moveable probe can be placed in bottom, top, and side ports. The time responses of the moveable probe are a few μsec for V_f measurements and about 10 μsec for T_e measurements; however, the probe does not recover well from large, fast V_f spikes or arcs. The sheath potential is roughly three times the local electron temperature. The edge density has not been measured with probes during start-up for this series of observations.

For both the moveable probe near the wall and the fixed probe on the separatrix, the signals have large fluctuations for up to 700 μsec, then drop to a lower plateau value. By 1.2 msec the bridge probe gives $T_e \approx 20$ eV while a probe located 1.5 cm from the bottom wall gives $T_e = 5$ eV and $V_f \approx 20$ to 30 volts. The edge density probably falls from the initial uniform filling density of about $5 \times 10^{12} cm^{-3}$ to its plateau value (at t=3.0 msec) of about $3 \times 10^{11} cm^{-3}$ at 2.5 cm from the wall and about $3.2 \times 10^{12} cm^{-3}$ near the separatrix.[6] Before the plateau phase T_e and V_f show several large spikes, with T_e reaching 60 eV on the separatrix and 40 eV near the wall, while V_f at the wall reaches 250 volts, as shown in Figure 6-1. On JFT-2 double probe characteristics show similar values for T_e and V_f (up to a factor of two higher) at the spike and include electron density measurements roughly 3 times higher at the peak of the spike relative to the steady-state value.[7] Since the time response for the T_e measurement on Tokapole II is not adequate, these numbers may be viewed as showing the trends in T_e only; however, the shot-to-shot reproducibility for the same plasma

conditions is within 20% even at the spikes for a particular run day. Figure 6-1 shows the effects of titanium coating between shots. Since the machine is not normally gettered, the coating technique effectively reduces the impurity concentration on the wall. No effects on loop voltage, n_e, or the discharge length are observed. The oxygen concentration decreases by about a factor of two at the ionization peak. With fewer wall impurities released into the plasma, V_f on the probe located 1.5 cm from the bottom wall increases at some of the spikes by 20% to 50%. The T_e changes on this probe are time-dependent with the initial spike apparently reduced about 20%. A factor of two difference in low-Z impurity concentration does not change the edge parameters enough to establish clear trends.

A great deal of work has already been done to compare Tokapole plasmas with and without ECRH preionization, with the primary result being that ECRH can reduce the loop voltage by a factor of two.[3] For the data presented in this section the 5 Gauss d.c. vertical field has been used for the best optimized, standard case. A comparison of three cases has been used to identify trends in impurity production: the standard case (with K-band preionization and the d.c. vertical field), the no K-band case (with vertical field), and the no d.c. vertical field case (with K-band). The time-dependences of probe T_e and V_f signals have been compared for the standard case of Figure 6-1 and the no K-band case. Typical signals are shown in Figure 6-2. Since the no K-band case breaks

Figure 6-1. The solid line is the standard case (with d.c. vertical field and K-band); the dashed line is the same case after an hour of slow titanium evaporation.

a. V_f versus time on a probe located 1.5 cm from the bottom wall.

b. T_e versus time for the same probe and shots. Note that during an arc to the probe, V_f does not respond well and thus the derived T_e can be negative. These unphysical values are not shown.

c. OIII λ703 versus time.

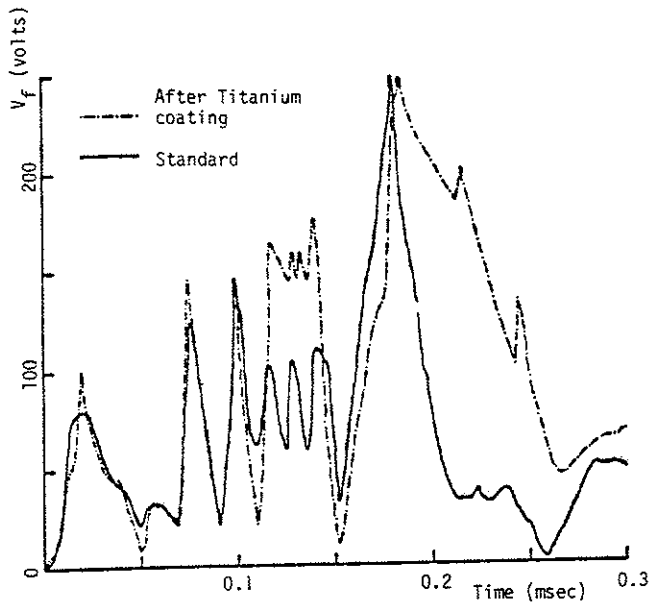

Floating Potential vs time

(Probe located 1.5 cm from bottom wall)

Figure 6-1a

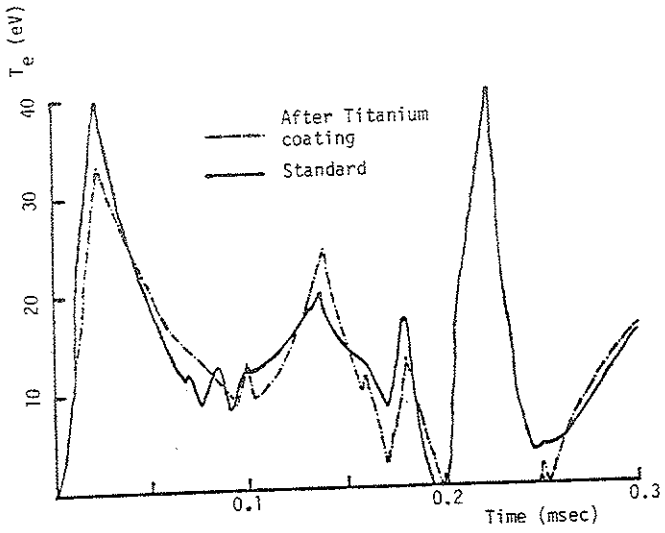

Te vs time

(Probe located 1.5 cm from wall)

Figure 6-1b

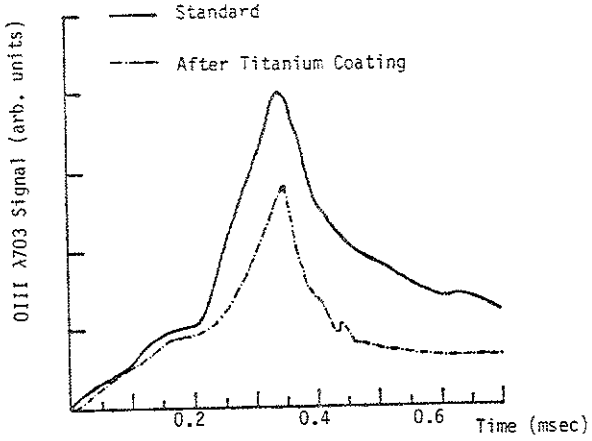

OIII λ703 vs time

Figure 6-1c

Figure 6-2. The solid line is the standard case; the dashed line is the no K-band case.

a. V_f versus time on the probe located 1.5 cm from the bottom wall, with the no K-band case time-adjusted.

b. T_e versus time for the same conditions as in a.

c. OIII λ703 versus time, with no time-adjustment.

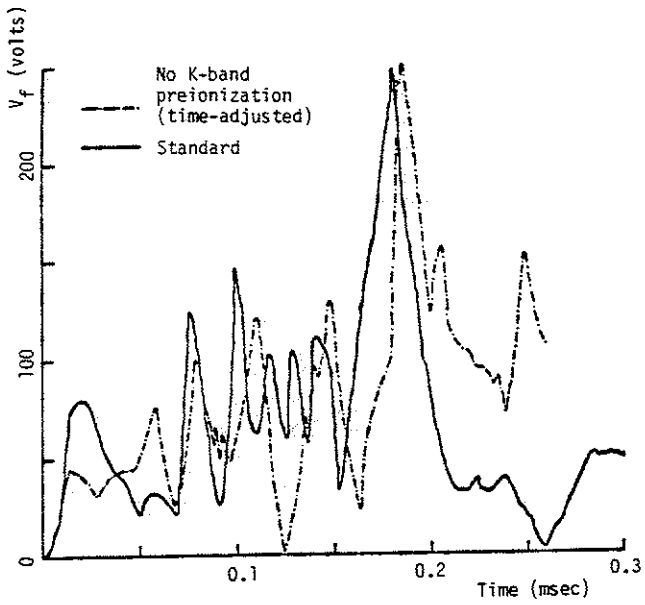

Floating Potential vs time

(Probe located 1.5 cm from bottom wall)

Figure 6-2a

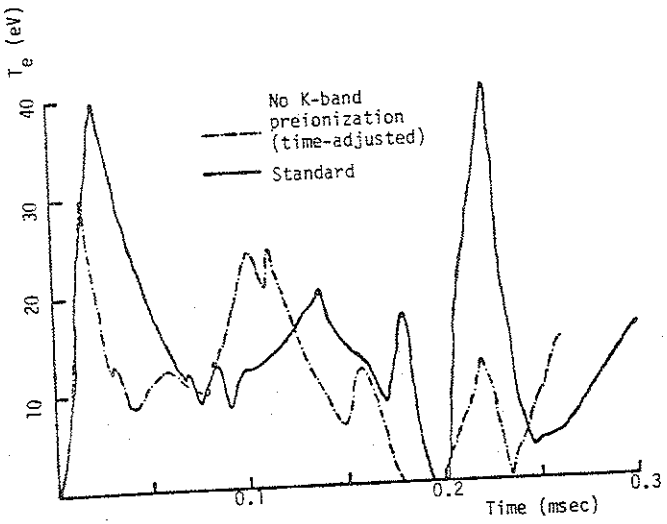

Te vs time

(Probe located 1.5 cm from bottom wall)

Figure 6-2b

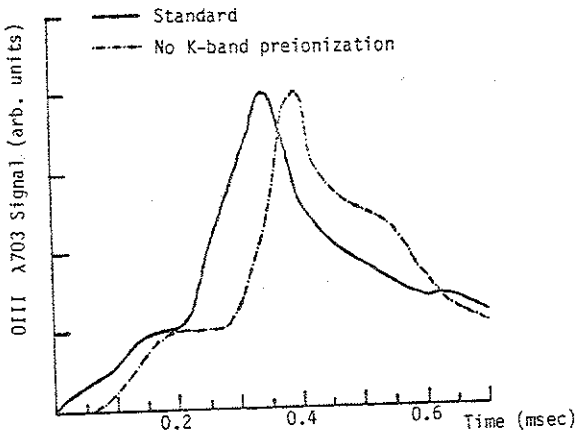

OIII λ703 vs time

Figure 6-2c

down later (causing n_e to peak later but at the same value), the early time dependence of spikes is not the same. The no K-band case is "time-adjusted" by matching the spike time at 250 μsec and the onset of the plateau at about 700 μsec. Figure 6-2c shows that the oxygen peak signals, not time-adjusted, have the same magnitude for the two cases. The first spike in T_e is clearly larger for the standard case, although the second spike is somewhat smaller. The V_f signal is similar, with the initial spike higher for the standard case, but the later spikes somewhat lower. These edge potentials and temperatures are consistent with ion-induced desorption thresholds and the lack of metal sputtering. The spikes do not seem to have a major effect on oxygen production.

The spikes may instead have a great deal to do with unipolar arcing; no definitive experiments have been conducted so far. As shown in the next section, the SXR signal is much higher for the standard case, somewhat lower for the no K-band case, and lowest for the no d.c. vertical field case. Unfortunately, the SXR signal is both a measure of the metal impurity levels and a measure of the electron temperature. A higher signal is consistent with higher electron temperature achieved with less metal impurity radiation, but the opposite could also be true. Profile measurements of a signal such as AlIII λ3602 are needed with simultaneous edge measurements. Figure 6-3 shows the electron temperature gradient measured from the side. For this run the largest spike occurs at about 150 μsec for the three cases. The gradient is steep, with T_e

Figure 6-3. T_e versus position of probe from the side wall. T_e is taken at the peak of the first large spike.

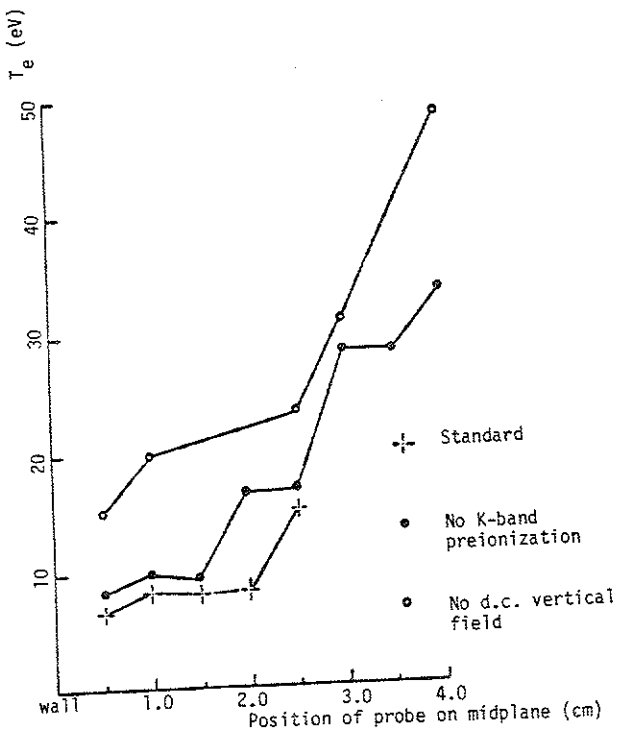

Te at t ≈ 150 μs (spike) vs Distance from wall

Figure 6-3

for the no d.c. vertical field case much higher. The trend for higher T_e in the no K-band case is probably not larger than the shot-to-shot error.

B. Impurity Profile Evolution

Spatial profiles of impurity radiation (OIII λ3760 and SXR signals) have been taken for many cases. The filter detectors may be rotated through ±25° from top center, side center, and bottom inner, center, and outer ports, as shown schematically in Figure 6-4. For the three cases of Section A the OIII λ3763 signals vary less than 30% for every chord. There is a trend for the no d.c. vertical field case to be the largest, the standard case to be slightly lower, and the no K-band case (unlike previous observations) to be the lowest.

For different plasma conditions, now optimized with K-band but with no d.c. vertical field, the oxygen profiles taken from four ports are shown in Figure 6-5. The signal at 200 μsec is the plateau value at the radiation barrier temperature. The ionization peak signal at 400 μsec shows essentially the same profile features. These features may be consistent with uniform distribution of oxygen in the tokamak region inside the separatrix.

The SXR profile is shown in Figure 6-6. This signal shows the tendency of the plasma to peak out from the midcylinder, especially for low I_p. A comparison of the plasma with and without the d.c. vertical field of Section A shows not only a large increase in the

Figure 6-4. Swivel ports available for profile scans, showing maximum angles of the scans. The top port is not shown.

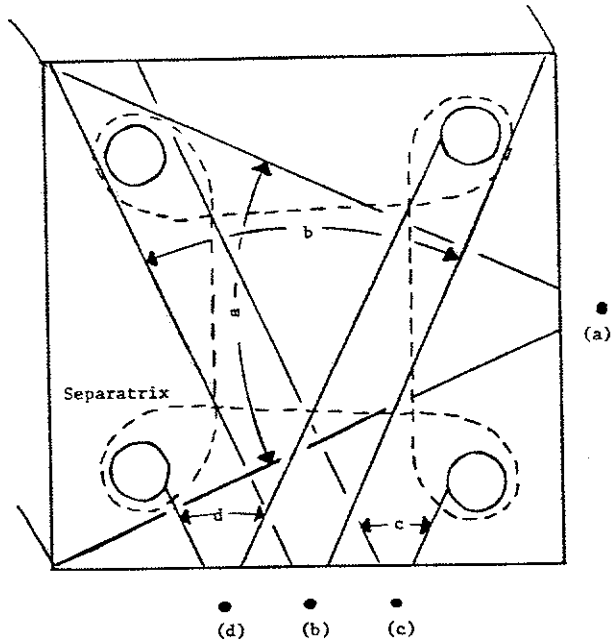

Tokapole II Swivel Ports Available for Profile Scan, Showing Maximum Angles

Figure 6-4

Figure 6-5. OIII λ3763 versus angle for the four ports shown: (a) side center, (b) bottom center, (c) bottom outer, and (d) bottom inner. The normalization is performed by dividing the signal by the length of the viewing chord, so that a uniform distribution in the machine would give a flat profile. The deviations from uniformity toward the rings may represent the differences in the octupole region.

a. At t = 200 μsec (when T_e ≈ 20 eV).

b. At t = 400 μsec (ionization peak time).

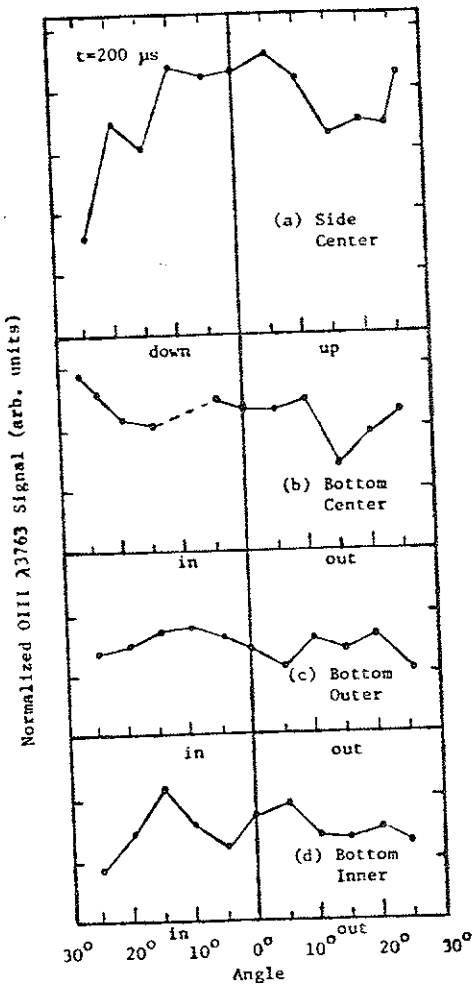

Figure 6-5a

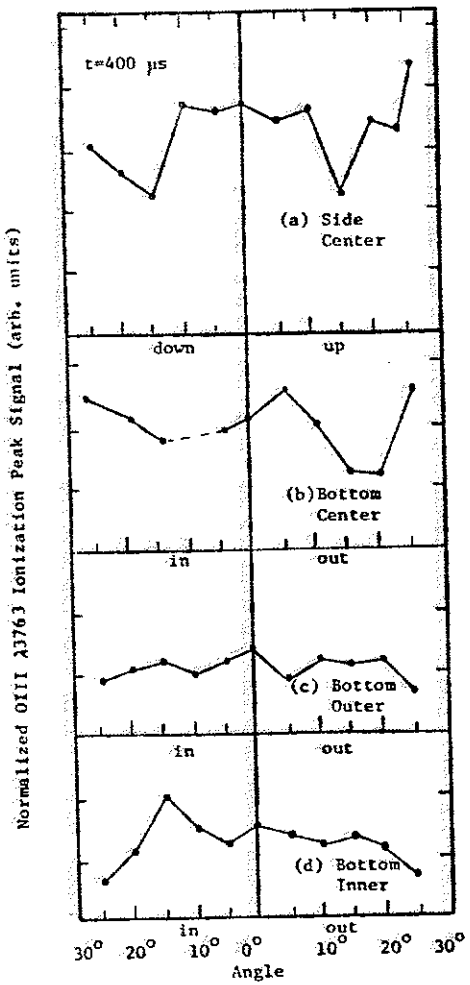

Figure 6-5b

Figure 6-6. SXR peak versus angle for low I_p case. The solid circles are for no d.c. vertical field case; the X's are for the standard case.

a. From the side center port.

b. From the top center port.

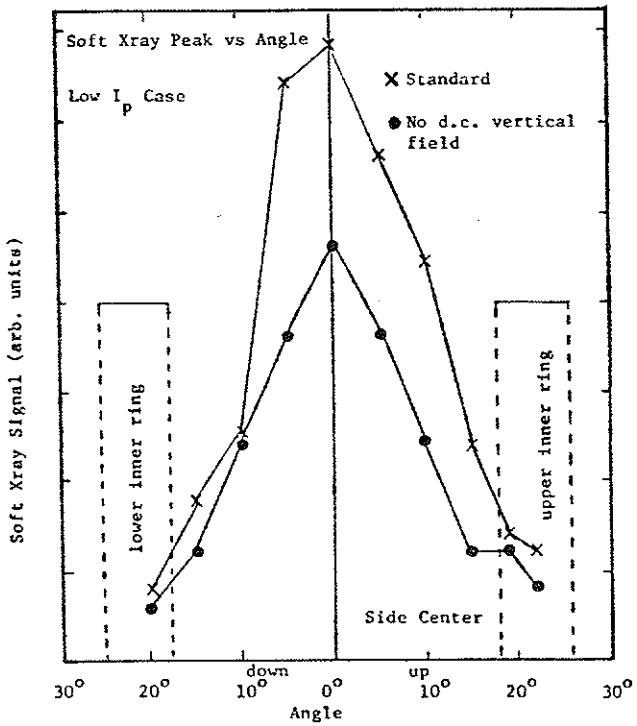

Figure 6-6a

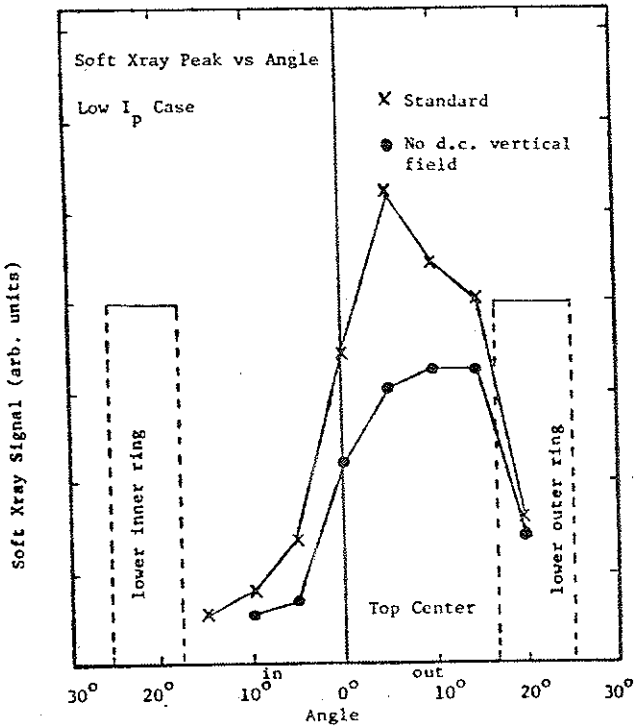

Figure 6-6b

SXR signal with d.c. vertical field, but also the ability of the vertical field to push the plasma back toward the center. Also shown are the peak and first sawtooth crash for a low I_p case and for a high I_p case (Figure 6-7). These cases imply that the sawtooth behavior, generally associated with the current profile, is clearly dependent upon the start-up procedure. More discussion of this behavior on Tokapole II is found in Reference 8. Presumably, programming the vertical field and the gas puff during start-up would be useful in controlling the profile evolution. Unfortunately, the vertical field soaks into the machine slowly and the start-up phase is too short for the puff valve to respond. The bad confinement of the start-up plasma and the large potentials at the walls are the major problems to be solved in order to reduce impurity production during start-up.

Figure 6-7. SXR versus angle from side center port, showing the peak (solid circles) and first sawtooth crash (open circles).

a. Low I_p case.

b. High I_p case.

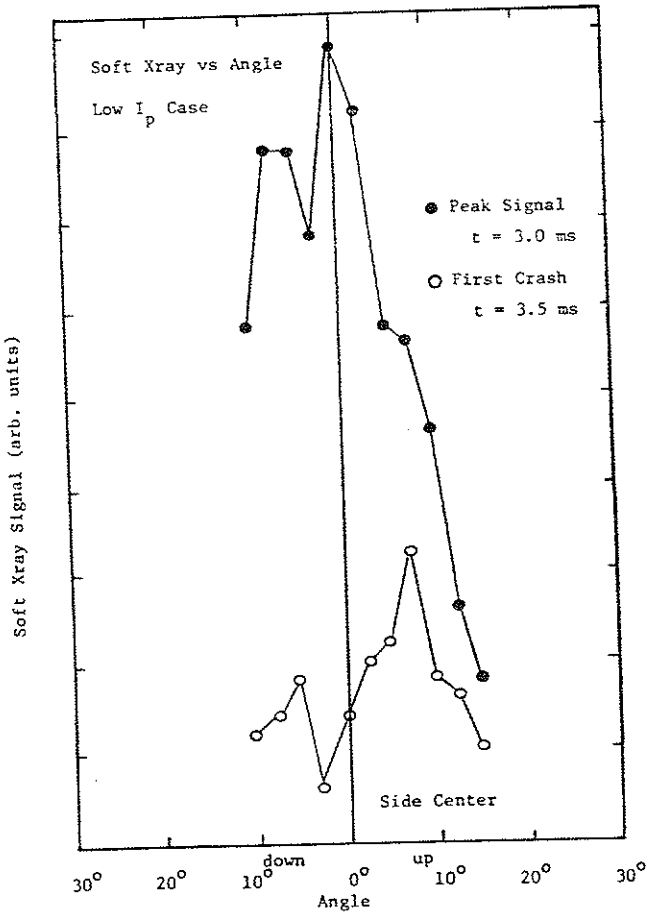

Figure 6-7a

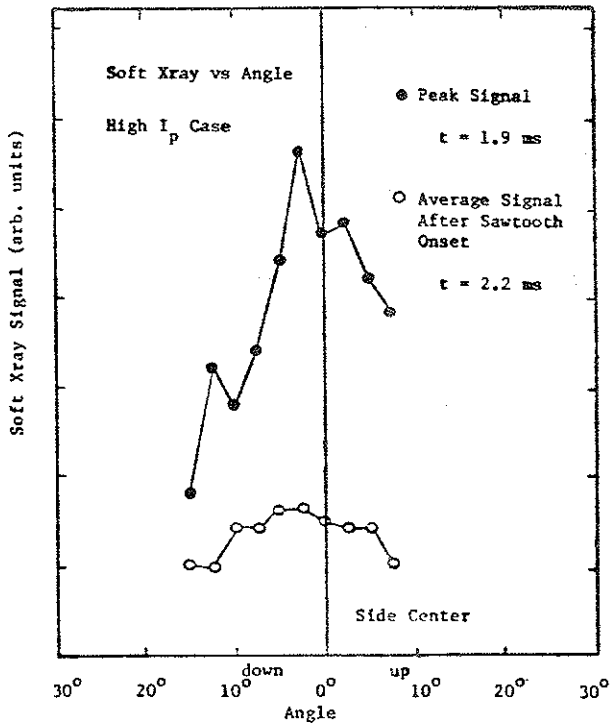

Figure 6-7b

REFERENCES

[1]G.M. McCracken, J. Nucl. Mater. 93/94 (1980) 3.

[2]R.M. Gilgenbach, M.E. Read, K.E. Hackett, R.F. Lucey, V.L. Granastein, et al., Nucl. Fusion 21 (1981) 319.

[3]D.J. Holly, S.C. Prager, D.A. Shepard, and J.C. Sprott, Nucl. Fusion 21 (1981) 1483.

[4]D.A. Shepard, private communication.

[5]J.C. Sprott, University of Wisconsin Plasma Studies PLP 109 (1967).

[6]T.D. Rempel and G.A. Emmert, University of Wisconsin Plasma Studies PLP 894 (1983).

[7]H.Ohtsuka, M. Maeno, N. Suzuki, S. Konoshima, S. Yamamoto, and N. Ogiwara, Nucl. Fusion 22 (1982) 823.

[8]T.H. Osborne and N.S. Brickhouse, University of Wisconsin Plasma Studies PLP 908 (1983).

CHAPTER 7

CONCLUSIONS AND DISCUSSION

Impurities in a tokamak plasma can affect the discharge in a variety of ways. Perhaps the most important and obvious problem is the radiation of input power. Although most tokamaks today operate without significant radiated power loss during the steady-state phase of the discharge, the start-up is slowed by both low-Z and high-Z impurity radiation. For Tokapole II this radiation may be a consumption of volt-seconds that could otherwise be used to heat the plasma to a higher temperature. Other impurity effects on Tokapole II discharges are perhaps more subtle, including modification of many parameters affecting equilibrium, stability, and transport.

To reduce impurity concentrations good vacuum and surface conditioning techniques are critical. Some recommendations for improving the overall cleanliness of Tokapole II plasmas have been included in this thesis. The vacuum materials (aluminum and copper), the internal divertor rings, and the frequent operation without limiter plates make the Tokapole II environment unique, so that tokamak cleaning lore may not directly apply. The reduction of low-Z impurities at start-up and the overall reduction of copper are reasonable goals for ultimately raising T_e.

Since some level of impurities is inevitable, this thesis has addressed the issue of impurity production. An understanding of the plasma loss mechanisms, the interaction of the plasma with the wall, and the recycling of impurities may give tokamak operators more control of the impurity effects.

A. Start-up

Much progress has been made in the understanding of impurity production during start-up. Ion-induced desorption has been identified as the primary mechanism for low-Z impurity production. The momentum exchange process has been demonstrated by the proportionality between the intrinsic low-Z impurity levels and the mass of the initial plasma during impurity doping and isotopic exchange experiments. Because very little data exists for low energy ion-induced desorption, the relationship between the desorption cross section and the mass of the incident ion is itself of interest.

The parameter σ/τ (desorption cross section divided by particle confinement time) has been determined from a time-dependent coronal model of the oxygen series ionization. Using the only available data for low energy desorption cross sections provides an estimate of the early particle confinement time. The energy of singly charged incident ions is estimated to be about 60 eV.

The metal impurity production mechanisms are less well understood. Since aluminum shows no increase with doped impurity concentration or mass, sputtering is probably not a dominant process. The sheath potential is somewhat below the sputtering threshold. Unipolar arcing is likely to be the cause of aluminum release, consistent with spikes observed in the sheath potential associated on other tokamaks with arcing. Copper production includes ion-induced sputtering or desorption, arcing and possibly direct bombardment of the ring supports by high energy electrons.

B. Steady-state

Much work remains to be done to understand the impurities in the Tokapole II steady-state plasma. The measured sheath potential at the wall is only about 20 eV with very little fluctuation activity after 700 μsec. By about this time the OIII signals have flat plateau values. Doping and titanium gettering can affect the ionization peak by as much as a factor of two without changing this plateau level. Once the oxygen on the wall is depleted during start-up, this constant level of oxygen in the plasma is maintained through recycling. The balance between loss and influx during the complicated recycling process seems remarkable. High energy, highly charged oxygen ions diffuse to the wall, knocking neutrals into the plasma. These neutrals in turn ionize, cool the edge by radiation, and thus reduce the sheath potential. The desorption and sputtering yields must decrease with the lower energy incoming ions.

Accumulation of metal impurities at the center is an alternate possibility which does not occur under normal Tokapole II conditions. Accumulation has been seen during late gas impurity puffing experiments, after which the discharge is quickly terminated, either by radiation losses or disruptions. Impurity puffing late in the discharge as a technique to study desorption and sputtering has not given reproducible results. Certainly the heavier mass gases are too slow coming into the machine for such short discharges. A comparison of H_2, D_2, and He may be possible if edge parameters and the recycling rates for each plasma species are measured simultaneously.

The spectroscopic signals continue to be useful diagnostics of the hot central plasma. Profiles of steady-state OIII have been quite consistent with the local T_e measured with probes, as expected from coronal equilibrium (assuming diffusion is a small term). Profiles of more highly charged oxygen ions should give an estimate of the T_e profile, but will require the tilting capability of the grazing incidence monochromator. These scans can then be compared with the broadband SXR profiles. For stability and fluctuation studies, these profiles may provide the basis for more localized information on density and temperature fluctuations. The metal impurity profiles will also be obtainable with the higher energy values available with this monochromator, making a study of metal impurity production more feasible.